nature communications

Article

https://doi.org/10.1038/s41467-024-54256-4

PPP1R2 stimulates protein phosphatase-1 through stabilisation of dynamic subunit interactions

Received: 17 May 2024

Accepted: 1 November 2024

Published online: 13 November 2024

Check for updates

Sarah Lemaire[1,5], Mónica Ferreira[1,5], Zander Claes[1,5], Rita Derua[2], Madryn Lake[1], Gerd Van der Hoeven[1], Fabienne Withof[1], Xinyu Cao[1], Elora C. Greiner[3,4], Arminja N. Kettenbach[3,4], Aleyde Van Eynde[1] & Mathieu Bollen[1]

Protein Ser/Thr phosphatase PP1 is always associated with one or two regulatory subunits or RIPPOs. One of the earliest evolved RIPPOs is PPP1R2, also known as Inhibitor-2. Since its discovery nearly 5 decades ago, PPP1R2 has been variously described as an inhibitor, activator or (metal) chaperone of PP1, but it is still unknown how PPP1R2 affects the function of PP1 in intact cells. Here, using specific research tools, we demonstrate that PPP1R2 stabilises a subgroup of PP1 holoenzymes, exemplified by PP1:RepoMan, thereby promoting the dephosphorylation of their substrates. Mechanistically, the recruitment of PPP1R2 disrupts an inhibitory, fuzzy interaction between the C-terminal tail and catalytic domain of PP1, and generates an additional C-terminal RepoMan-interaction site. The resulting holoenzyme is further stabilized by a direct PPP1R2:RepoMan interaction, which renders it refractory to competitive disruption by RIPPOs that do not interact with PPP1R2. Our data demonstrate that PPP1R2 modulates the function of PP1 by altering the balance between holoenzymes through stabilisation of specific subunit interactions.

Protein phosphatase-1 (PP1) belongs to the PPP-family of protein Ser/Thr phosphatases[1]. It is present in all eukaryotic cells and dephosphorylates a large variety of phosphoproteins. PP1 has a globular catalytic domain with two metals (Zn^{2+} and Fe^{2+}) in its active site that are essential for catalysis[2,3]. The catalytic domain is also characterized by C-terminal, hydrophobic and acidic surface grooves that emanate from the active site and function as docking sites for substrates and inhibitors. PP1 is regulated by a huge diversity (≈200 in mammals) of structurally unrelated Regulatory-Interactors-of-Protein-Phosphatase-One (RIPPOs)[1,4,5]. RIPPOs control PP1 through occlusion of the active site, interference with substrate selection, and/or targeting to a specific subcellular location. Conversely, PP1 often regulates associated RIPPOs through dephosphorylation of key regulatory Ser/Thr residues[5]. Most RIPPOs have a disordered PP1-binding domain with several short linear motifs (SLiMs) that create a large interaction interface for the catalytic domain of PP1. Widespread PP1-anchoring SLiMs include the so-called RVxF and SILK motifs. Some RIPPOs, such as the MYPT and ASSP proteins, have an additional, structured PP1-binding domain that interacts with the disordered C-terminal tail of PP1[6,7]. RIPPOs are globally much more abundant than PP1 and they dynamically compete with each other for binding with PP1 via their shared RVxF motif[4]. Hence, the set of PP1:RIPPO complexes that accumulates in cells is, at least partially, determined by the relative concentration of RIPPOs and their (regulated) affinity for PP1.

PPP1R2 (R2), also known as Inhibitor 2, IPP2 or PP1-modulator protein, is an early evolved RIPPO that is expressed in all plants,

[1]Laboratory of Biosignaling & Therapeutics, KU Leuven Department of Cellular and Molecular Medicine, University of Leuven, Leuven, Belgium. [2]Laboratory of Protein Phosphorylation & Proteomics, KU Leuven Department of Cellular and Molecular Medicine, University of Leuven, Leuven, Belgium. [3]Department of Biochemistry and Cell Biology, Geisel School of Medicine at Dartmouth, Hanover, NH, USA. [4]Dartmouth Cancer Center, Lebanon, NH, USA. [5]These authors contributed equally: Sarah Lemaire, Mónica Ferreira, Zander Claes. e-mail: Mathieu.Bollen@kuleuven.be

animals, fungi and photosynthesizing algae[8,9], hinting at a conserved function in the regulation of PP1. Yet, nearly 50 years after its discovery[10], it is still an enigma how R2 actually regulates PP1, as a broad array of structural, biochemical, and deletion/overexpression studies yielded conflicting results (reviewed by Lemaire and Bollen[9]). R2 has little stable secondary structure in its unbound form and does not alter the conformation of the catalytic domain of associated PP1[11,12]. In addition, the C-terminal tail of PP1 is invisible in PP1:R2 crystal structures, indicating that it remains disordered[12]. In the PP1:R2 complex, R2 binds to PP1 via RVxF and SILK motifs as well as a unique helical IDoHA motif that binds to the hydrophobic and acidic grooves of PP1. Within this IDoHA motif, a conserved HYNE-sequence occludes the active site. R2 can also form ternary complexes with PP1 and a second RIPPO, such as Neurabin[13,14]. In the ternary R2:PP1:Neurabin complex, the binding of R2 to PP1 via its degenerate RVxF motif is outcompeted by the canonical RVxF-motif of Neurabin, leaving only the SILK and IDoHA motifs for interaction with PP1. The crystal structure of PP1:R2 suggests that R2 is inhibitory for PP1 as the active site is occluded by the HYNE sequence[12]. Purified and transiently overexpressed R2 indeed functions as a potent (competitive) PP1 inhibitor ($K_{d1} \approx 5$ nM). However, R2 is only inhibitory for a subset of substrates and is still inhibitory after deletion of the IDoHA motif[15,16], indicating that it does not (solely) inhibit PP1 by blocking access to the active site. Moreover, at non-inhibitory concentrations ($K_{d2} \approx 0.5$ nM), R2 still forms a heterodimeric complex with PP1 that is fully active, arguing against constitutive obstruction of the active site by the IDoHA motif (reviewed by Lemaire and Bollen[9]). Nevertheless, this active PP1:R2 complex gradually loses its activity upon further incubation. The resulting inactive complex is often referred to as the MgATP-dependent phosphatase because it can be re-activated by transient phosphorylation of R2 at Thr73 by a proline-directed kinase. R2-inactivated PP1 can also be re-activated by metal addition following the removal of R2, indicating that R2 functions as a PP1 chaperone for metal (un)loading. Consistent with this notion, bacterially expressed PP1, which has two active-site metals (Mn^{2+}) and a substrate specificity that differs from that of native PP1, can be converted to a native-like enzyme by a cycle of R2-mediated inactivation and re-activation[15]. At present, there is no conclusive evidence for the existence of a pool of R2-inactivated PP1 in intact cells[17–20]. The available data rather suggest that the MgATP-dependent PP1:R2 heterodimer is only formed after cell lysis (reviewed by Lemaire and Bollen[9]). Finally, R2-depletion studies indicate that R2 functions as a PP1 activator, as its removal results in the hyper-phosphorylation of established PP1 substrates[21,22]. The mechanism underlying this putative PP1-activatory function of R2 is not known. A further complication in understanding the biological function of R2 is that it also acts, at least in vitro, as an allosteric regulator of protein kinase Aurora A and prolyl isomerase Pin1 [23,24].

Here, using specific cell lines and protein-interaction assays, we demonstrate that R2 stimulates a subset of PP1 holoenzymes, including PP1:RepoMan, by a mechanism that is strictly dependent on its direct interaction with PP1. Structural analysis shows that R2 binding remodels the RVxF-docking site on PP1, thereby creating an extended RIPPO-interaction surface formed by R2 and the C-terminal tail of PP1. We furthermore demonstrate that PP1:RepoMan is stabilized by R2 recruitment, which renders the complex refractory to competitive disruption by RIPPOs that do not interact with R2 and the C-terminal tail of PP1. Our data provide key molecular insights in the regulation of PP1 by R2 and offer a rationale for explaining discrepancies in the R2 literature.

Results

The depletion of R2 results in reduced cell proliferation

To explore the role of R2 in mammalian cells, we used CRISPR/Cas9 to edit the *PPP1R2* alleles in the human HCT116 colorectal carcinoma-cell line to encode for a R2-mAID-mClover fusion, enabling its inducible proteolytic degradation by the addition of doxycyclin (Dox) and Indol-3-Acetic Acid (IAA) (Fig. 1a)[25]. The R2-mAID-mClover fusion showed a strong nuclear enrichment in interphase cells (Fig. 1b), in accordance with published data on the subcellular distribution of endogenous R2[26]. In mitotic cells, the R2 fusion was slightly enriched at the spindle and kinetochores during (pro)metaphase. Despite identical transcript levels for R2-WT (parental cells) and R2-mAID-mClover (R2-degron cells) (Supplementary Fig. 1a), the R2-mAID-mClover protein expression level in the non-induced cells appeared to be much higher than that of R2-WT, as detected by immunoblotting with R2-specific antibodies (Fig. 1c). However, this increased immunodetection of the R2 fusion was caused by its enhanced adherence to the PVDF membrane, as TEV-cleavage of transiently expressed R2-mAID-mClover with a TEV-cleavage site between R2 and mAID-mClover reduced immunodetected R2 to normal levels (Supplementary Fig. 1b).

The degradation of R2-mAID-mClover, induced by Dox/IAA addition (Fig. 1a), was maximal 48 h after Dox/IAA addition, as shown by both immunoblotting (Fig. 1c and Supplementary Fig. 1c) and mClover-fluorescence imaging (Supplementary Fig. 1d). Dox/IAA addition did not affect the R2 level in the parental cell line (Fig. 1c). A washout of Dox/IAA in the R2-depleted degron cell line resulted in the re-appearance of R2-mAID-mClover after 24 h (Fig. 1c), attesting to the reversibility of R2 depletion. Following Dox/IAA-induced degradation of R2-mAID-mClover, the cell-proliferation rate in SRB assays was reduced by half (Fig. 1d). This accords with data from genome-wide CRISPR deletion screens, showing that R2 is essential for the proliferation of 837 out of 1150 examined cancer-cell lines[27]. Dox/IAA addition only had a minor effect on the proliferation of the parental cell line. The decreased proliferation of R2-depleted cells was not associated with a specific cell-cycle arrest, as indicated by flow-cytometry analysis of unsynchronized cells (Supplementary Fig. 1e) or cells that were released from a thymidine arrest (Supplementary Fig. 1f and 1g). Neither did time-lapse video imaging disclose an abnormal mitotic progression of R2-depleted cells (Supplementary Fig. 1h). Hence, our data demonstrated that R2 is a determinant of cell proliferation but does not affect progression through a specific phase of the cell cycle.

R2 depletion results in hyper-phosphorylation of a subset of PP1 substrates

We subsequently examined the effects of R2 depletion on PP1 and the phosphorylation status of its substrates. The expression levels of the PP1α, PP1β and PP1γ were not affected by R2 depletion (Fig. 2a). To assess the effect of R2 depletion on the activity of PP1, we partially purified PP1 from cell lysates using a protocol that separates PP1 from associated RIPPOs and other phosphatases (Supplementary Fig. 2a and 2b)[28]. The activity of PP1 purified from parental and R2-depleted cells, assayed with glycogen phosphorylase *a* as substrate, was not significantly different (Fig. 2b), demonstrating that R2 depletion did not affect the specific enzymatic activity of PP1 resulting, for example, from metal loss at the active site. We verified that the observed dephosphorylation stemmed from PP1, as it was completely blocked by the addition of NIPP1, a selective PP1-inhibiting RIPPO[29]. A global phosphoproteome analysis of the parental and R2-depleted HCT116 cells led to the identification of 2450 hyper-phosphorylated and 925 hypo-phosphorylated tryptic peptides in R2-depleted cells (Fig. 2c and Supplementary Data 1), indicating that R2 depletion mainly resulted in protein hyperphosphorylation. After implementation of an FDR of 0.2, we also detected more hyperphosphorylated (775) than hypophosphorylated (402) peptides after R2 depletion (Supplementary Fig. 2c; Supplementary data 1). Protein hyperphosphorylation in R2-depleted cells was also more prevalent when the analysis was limited to established PP1 substrates, as derived from the DEPOD protein dephosphorylation database (https://depod.bioss.uni-freiburg.de; Supplementary Fig. 2d). A gene-ontology enrichment analysis revealed

https://doi.org/10.1038/s41467-024-54256-4

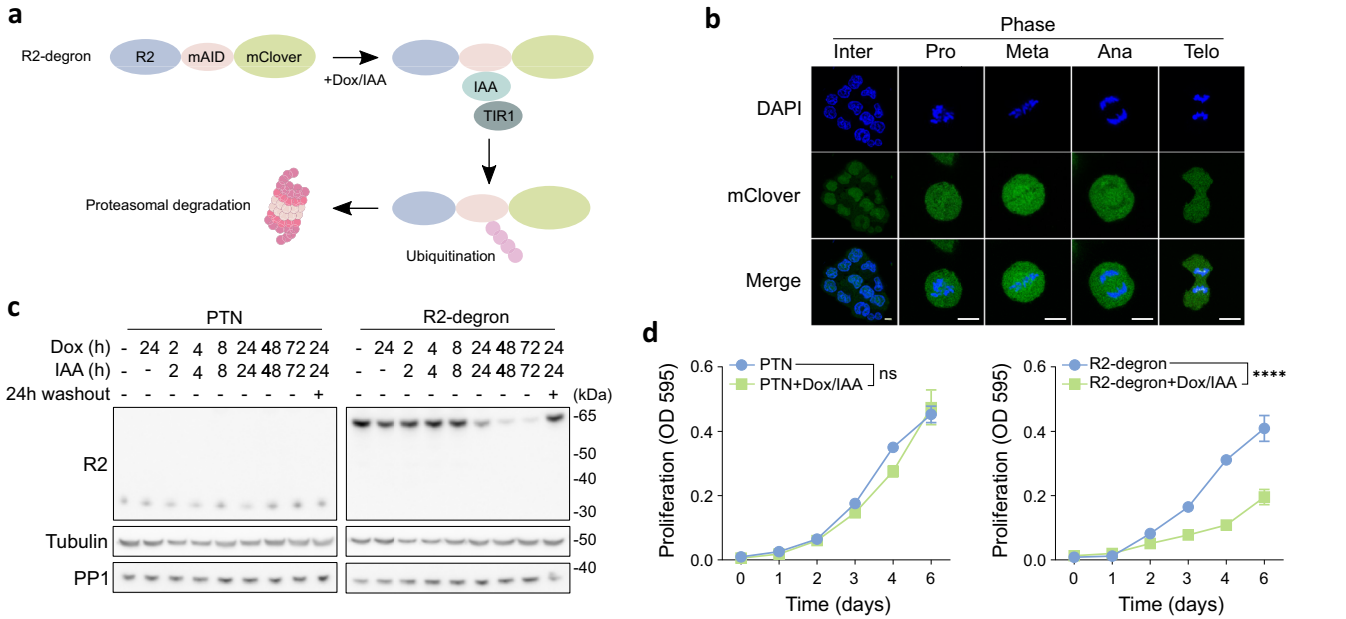

Fig. 1 | Reduced proliferation of HCT116-degron cells after R2 depletion. **a** Scheme of Dox/IAA-induced degradation of R2 in the HCT116-degron cell line. **b** Localization of R2-mAID-mClover in untreated R2-degron cells. Fixed cells were analysed for mClover-fluorescence and stained with DAPI. Scale bars are 10 μm. **c** Parental (PTN) and R2-degron cells were incubated for the indicated time points with 2 μg/ml Doxycycline (Dox) and/or 500 μM IAA. The panel shows the time-dependent degradation of R2-mAID-mClover in the R2-degron cell line and the re-appearance of R2-mAID-mClover after drug washout. Tubulin and PP1 were used as loading controls. This is a representative experiment of three biological repeats. **d** Cell-proliferation rate of PTN and R2-degron cells, before and after Dox/IAA treatment, as derived from sulforhodamine B (SRB) assays. A non-linear regression analysis was conducted to compare proliferation curves between untreated and treated conditions over multiple time points, the significance level is indicated (****, $P < 0.0001$). The data represents the mean values ± SD of 6 technical repeats.

that R2 depletion mainly affected the phosphorylation of proteins that regulate nuclear processes such as transcription, mRNA processing and chromatin organization (Fig. 2d), consistent with the predominant nuclear localization of R2 (Fig. 1b). We subsequently investigated the effect of R2 depletion on specific PP1 substrates. In the first half of mitosis, the C-terminal tail of PP1 is phosphorylated by CDK1 at a conserved residue (Thr320 for PP1α) that is auto-dephosphorylated at the mitotic exit[30,31]. We noted a severalfold increased phosphorylation of PP1α at Thr320 in G_2/M-arrested (RO3306 addition) R2-depleted cells, and this increase was maintained for 2 h after RO3306-washout (Fig. 2e, f). The phosphorylation of histone H3 at Thr3 (H3T3), a substrate of PP1:RepoMan, was also increased after R2 depletion (Fig. 2e, g, Supplementary Fig. 2e and 2f, Supplementary note 1). However, other established substrates of PP1, including Thr412 of RepoMan and Ser780 of Retinoblastoma protein, did not show a differential phosphorylation (Supplementary Fig. 2g). To distinguish between an effect of R2 depletion on the activity of PP1 or a counteracting kinase, we performed a kinase shutoff assay in intact cells and monitored the dephosphorylation rate of PP1α at Thr320 (Fig. 2h). PP1 was first hyperphosphorylated following a treatment of HCT116 cells with calyculin A, an inhibitor of PPP-type phosphatases. Thr320 was rapidly dephosphorylated after calyculin-A washout and addition of staurosporin, a general kinase inhibitor. Importantly, PP1 dephosphorylation occurred much more slowly in the absence of R2, indicating that the hyperphosphorylation of PP1 substrates was caused by a decrease in PP1 activity, rather than an increase in kinase activity. Together, these data indicated that R2 is a positive regulator of a subset of PP1 holoenzymes.

Knock-in of a PP1-binding mutant of R2 recapitulates the phenotype of R2 depletion

To explore the molecular mechanism underlying the stimulation of PP1 holoenzymes by R2, we first examined to which extent this function of R2 was dependent on its direct interaction with PP1. R2 has several PP1-binding motifs (Fig. 3a)[12]. To delineate the relative importance of these motifs for PP1 binding, we generated single and combined mutations of these motifs in an EGFP-R2 fusion. PP1 immunoblotting of EGFP-traps of the transiently expressed R2 fusions showed that the single or combined mutation of the SILK (GILK → GAAA) and RVxF motifs (SQKW → SAKA) only partially disrupted the PP1:R2 interaction (Fig. 3b, c). However, mutation of the HYNE-sequence (HYNE→AAAA) within the IDoHA motif completely abolished the PP1:R2 interaction. Next, we obtained HCT116 cell lines (2 independent clones) where this mutation of the HYNE-sequence was introduced in both *PPP1R2* alleles (HYNE→AAAA; R2-HYNEm) (Fig. 3d). We verified that R2-WT and R2-HYNEm were expressed at a similar level in the knock-in cell lines and that R2-HYNEm, in contrast to R2-WT, was not associated with immunoprecipitated PP1 (Supplementary Fig. 3a). Strikingly, the R2-HYNEm knock-in cell lines showed essentially the same phenotype as the R2-depleted degron cell line (Figs. 1 and 2) with respect to reduced cell proliferation (Fig. 3e and Supplementary Fig. 3b, c) and hyperphosphorylation of PP1 (Fig. 3f, g) and H3T3 (Fig. 3f, h). However, the phenotype of the R2-HYNEm knockin cell line was generally somewhat less severe than that of the R2-depleted degron cells (Figs. 1 and 2). These data demonstrated that the stimulation of PP1 holoenzymes by R2 is critically dependent on its direct interaction with PP1.

R2 is a component of a subgroup of PP1 holoenzymes

To identify the PP1 holoenzymes that are regulated by R2 in HCT116 cells, we determined the interactome of trapped R2-mAID-mClover by mass spectrometry. R2-mAID-mClover expressing HCT116 cells were either synchronized in prometaphase (nocodazole addition) or in early interphase (nocodazole washout for 4 h) (Fig. 4a). We identified 117 and 53 protein interactors of R2-mAID-mClover in mitosis and interphase, respectively (Supplementary Data 2). These interactors included 3 PP1 isoforms, 11 RIPPOs and 11 established RIPPO-interacting proteins (Fig. 4b, c). The RIPPOs interacting with R2 in prometaphase and early interphase were remarkably similar, except for RIF1 and eIF2β, which only interacted with R2 in interphase and mitosis,

https://doi.org/10.1038/s41467-024-54256-4

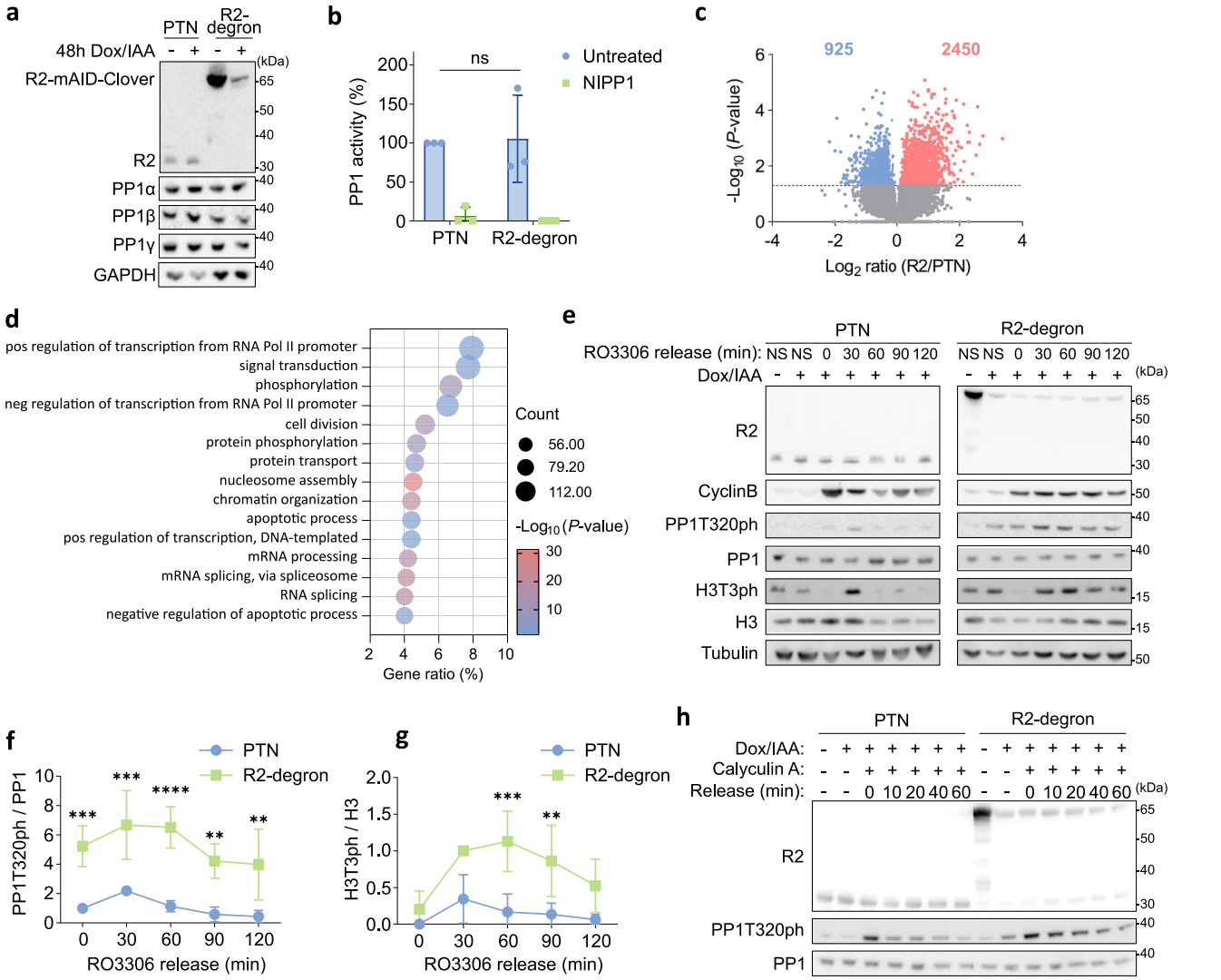

Fig. 2 | Protein hyper-phosphorylation in R2-depleted HCT116 cells. a The depletion of R2-mAID-mClover does not affect PP1 levels. GAPDH was used as loading control. Representative of 2 biological repeats. **b** PP1, purified from PTN and R2-degron cells, was assayed with phosphorylase *a* as substrate, with or without 1.35 nM NIPP1. A Two-Way ANOVA with Sidak's multiple comparisons did not disclose significant differences (ns). The data represent the means ± SD for 3 biological repeats. **c** Volcano plot of the phosphoproteome of R2-depleted HCT116 cells as compared to Dox/IAA-treated parental cells. The colored dots show different values ($P \leq 0.05$) in two-tailed Student's t-test. **d** Gene-ontology pathway analysis (DAVID) of the phosphoproteome in R2-depleted cells (the full human proteome was used as a background in the analysis). **e** PTN and R2-degron cells, treated −/+ Dox/IAA, were non-synchronized (NS) or synchronized at the G_2/M transition with RO3306. The time points indicate the washout from RO3306. Cell lysates were prepared in the presence of phosphatase inhibitors and used for immunoblotting. Tubulin was used as loading control. Representative image of 3 biological repeats. **f** Quantification of PP1T320ph (means ± SD; n = 3 biological repeats) for the experiment shown in panel (**e**). A multiple unpaired t-test was used to compare differences between PTN and R2-degron cell lines: **, $P \leq 0.01$; ***, $P \leq 0.001$; ****, $P \leq 0.0001$. **g** Quantification of H3T3ph (means ± SD; n = 3 biological repeats). A multiple unpaired t-test was used to compare differences between PTN and R2-degron cell lines: **, $P \leq 0.01$; ***, $P \leq 0.001$; ****, $P \leq 0.0001$. **h** Kinase-shutoff assay in PTN and R2-degron cells. Cells were treated with Dox/IAA for 48 h prior to calyculin-A treatment (25 nM for 30 min). Subsequently, the cells were released in medium with 10 μM staurosporine to allow dephosphorylation by endogenous phosphatases. At the indicated time points before and after calyculin-A washout, cell lysates were probed for R2, PP1 and PP1T320ph. Representative image of 2 biological repeats.

respectively. One of the identified R2-interacting RIPPOs was Neurabin-2 (Spinophilin), which is already known to form a ternary complex with PP1 and R2[13,14]. A large fraction of R2 interactors in HCT116 cells were established components of just a few macromolecular PP1 complexes, including the GCN2/eIF2β complex (eIF2α, eIF2β, eiF2γ, GCN2, PP1), the PNUTS/PTW complex (PNUTS, PP1, TOX4, WDR82), the RepoMan complex (PPP2R5/B56, PP1, RepoMan) and the URI/PPP1R19 complex (ASDURF, PDRG1, PFDN2, PFDN6, POLR2E, PP1, RPAP3, URI, UXT) (Fig. 4c). We confirmed the presence of PP1, URI, PNUTS and RepoMan in EGFP-trapped R2 by immunoblot analysis (Fig. 4d). Conversely, R2 was also present in a trap of transiently expressed EGFP-RepoMan-WT (Fig. 4e). However, R2 was not detected in traps of EGFP-RepoMan-RATA, in which the essential PP1-binding RVxF-motif of RepoMan was inactivated (^{392}RVTF^{395} → RATA). This indicated that the interaction of R2 with RepoMan was (largely) mediated by PP1, similar to its interaction mode in the R2:PP1:Neurabin complex[13,14]. R2 depletion did not affect the level of RepoMan (Supplementary Fig. 4a), which varies considerably during the cell cycle and is maximal during mitosis[32]. This demonstrated that R2 did not stimulate PP1:RepoMan by increasing the levels of RepoMan. Together, these data identified a subset of PP1:RIPPO complexes that interact with R2, but did not disclose how this interaction altered their activity.

https://doi.org/10.1038/s41467-024-54256-4

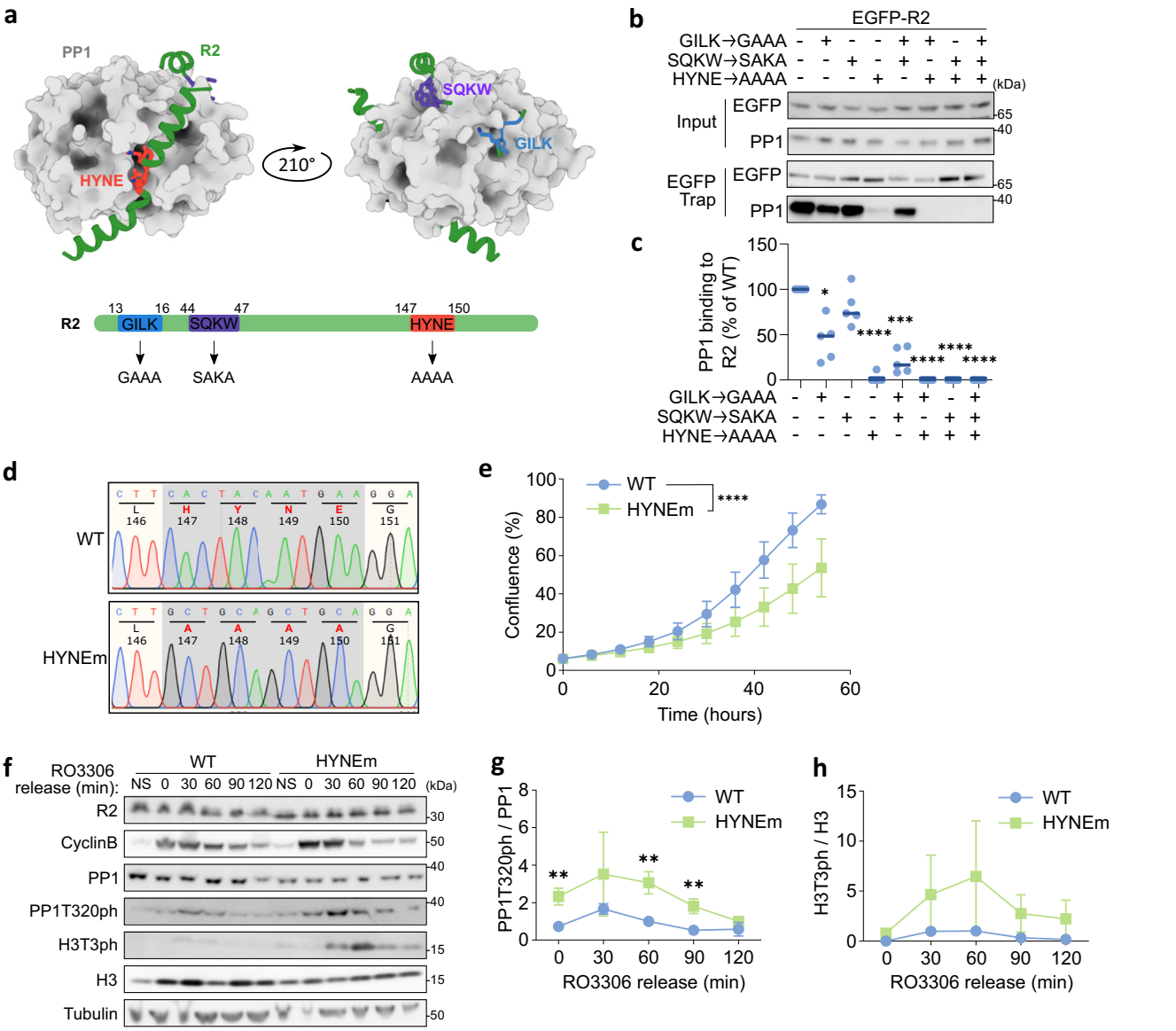

Fig. 3 | A R2-HYNEm knock-in recapitulates the phenotype of R2 depletion. **a** Crystal structure of PP1:R2 (PDB 2O8A) with the known PP1-binding motifs marked (upper panel). The position of the specific SILK (GILK) and RVxF (SQKW) sequences of R2 are shown as well as the HYNE sequence within the IDoHA motif. Also shown is the position of these motifs within R2 and the generated R2 mutants (m) (lower panel). **b** Traps of the indicated EGFP-tagged R2 variants, transiently expressed in HEK293T cells, were analysed for the presence of PP1. **c** Quantification of the data shown in panel (**b**). Results are means ± SD for n = 5 biological repeats. A One-Way ANOVA with Dunnett's multiple comparisons test was performed (*, $P \le 0.05$; ***, $P \le 0.001$; ****, $P \le 0.0001$). **d** Validation of one of two generated HYNEm HCT116 knock-in cell lines by DNA-sequence analysis of the PCR products that amplified the indicated R2 fragment. **e** Cell proliferation of the WT and HYNEm knock-in cell lines, as derived from IncuCyte analysis. The average of two different clones was used (data represents mean ± SD for n = 3 biological repeats per clone). A non-linear regression analysis was conducted to compare proliferation curves between untreated and treated conditions over multiple time points, the significance level is indicated (****, $P \le 0.0001$). **f** WT and HYNEm-knock-in cells, treated ± Dox/IAA, were non-synchronized (NS) or synchronized at the G_2/M transition with RO3306. The time points indicate the washout from RO3306. Cell lysates were prepared in the presence of phosphatases inhibitors and processed for immunoblotting with the indicated antibodies. Representative image of 3 biological repeats. **g** Quantification of PP1T320ph (means ± SD; n = 3 biological repeats). A multiple unpaired t-test was used to compare differences between WT and HYNEm knock-in cell lines: **, $P < 0.01$. **h** Quantification of H3T3ph (means ± SD; n = 3 biological repeats).

R2 displaces the C-terminus of PP1 from the active site

The conformation of the catalytic domain of PP1 is identical in crystal structures of PP1 (PDB 4MOV) and PP1:R2 (PDB 2O8A, 2O8G), while the C-terminus is not resolved, probably because it is intrinsically disordered. However, we noted that the C-terminus of PP1 docked near the active site in PP1α models from various mammalian species in the AlphaFold Protein Structure Database (EMBL-EBI) (Fig. 5a). We further explored this notion in silico by simulating the behavior of the C-terminus with all-atom molecular dynamics simulations of full-length PP1α[33], starting from a conformation where the C-terminus is extended and not in contact with the catalytic domain. In all 6 simulations, the C-terminus readily collapsed onto the catalytic domain and remained associated through dynamic interactions (Supplementary Fig. 5a, b and Supplementary Data 3). In the majority (~66%) of the simulations, the C-terminus of PP1α bound to the active site region in a conformation that occludes access to the catalytic site and/or substrate-binding grooves (Fig. 5b, Supplementary Fig 5b). Interestingly, hydrogen-bond analysis of the C-terminal tail over the course of

https://doi.org/10.1038/s41467-024-54256-4

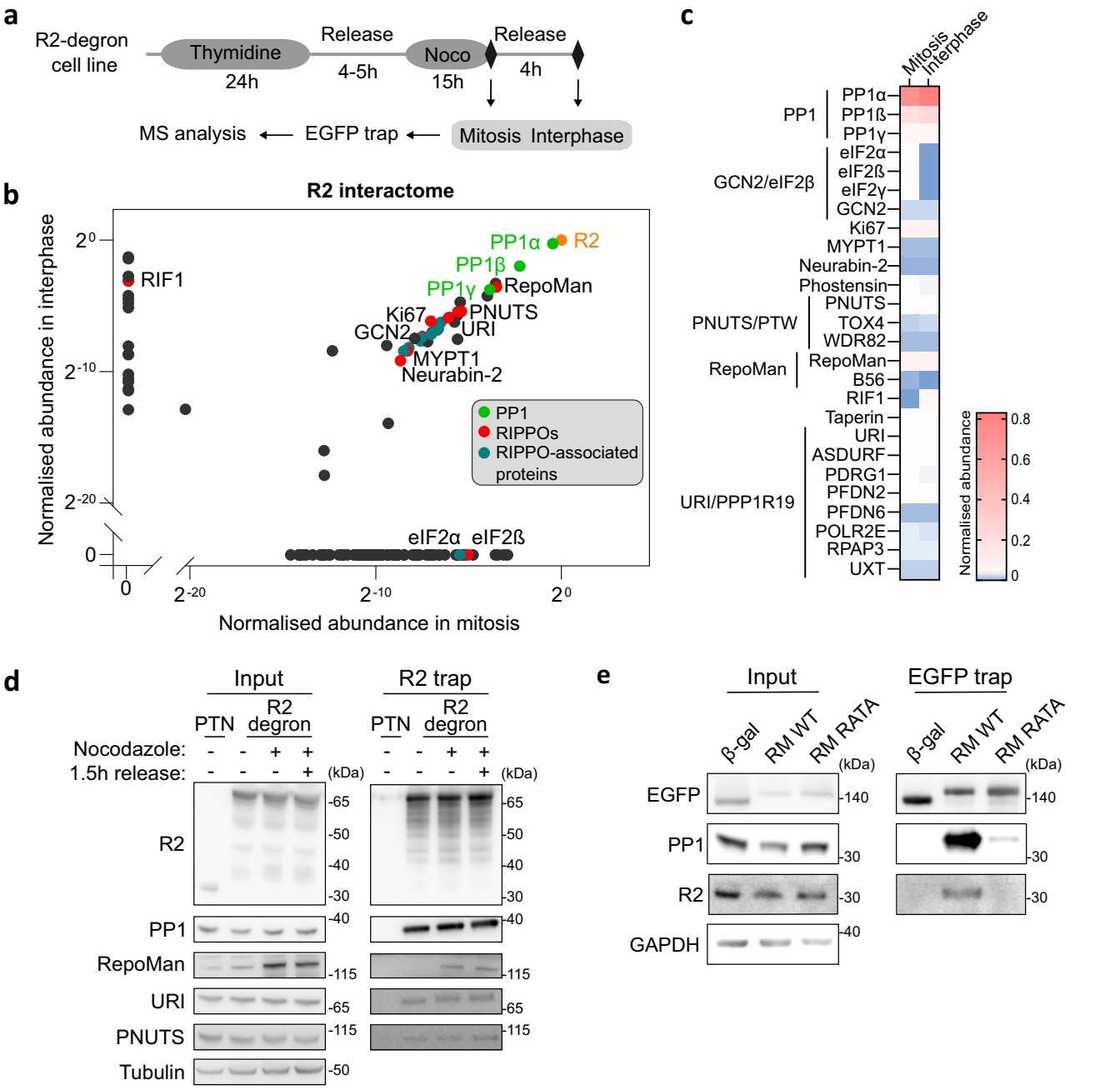

Fig. 4 | The interactome of R2-mAID-mClover in HCT116 cells. a Scheme for the synchronization of HCT116 R2-degron cells in mitosis and early interphase. EGFP-trapped R2-mAID-mClover was analyzed for interacting proteins by mass spectrometry (MS). **b** Normalized abundance of R2 interactors in mitosis and interphase. **c** Heatmap of R2-binding RIPPOs and RIPPO-interacting protein during mitosis and early interphase. **d** EGFP traps of R2-mAID-mClover from mitotically-arrested and released parental (PTN) and R2-degron cells confirmed the association of URI, RepoMan and PNUTS with R2-mAID-mClover. The binding of RepoMan was only detected during mitosis when RepoMan is most abundant. **e** Traps of EGFP-RepoMan (RM)-WT and the PP1-binding mutant EGFP-RM-RATA transiently expressed in HEK293T cells only show association of R2 with RepoMan-WT.

a representative simulation run indicated that most contacts with the catalytic domain were mediated by a conserved stretch of residues in the C-terminal tail (^{317}RPITPPR^{323}) (Supplementary Fig. 5c). The docking of the C-terminus of PP1 to its active-site region precludes the simultaneous binding of R2 via its IDoHA helix, as there is limited access to the acidic groove. An ensemble of 50 AlphaFold-Multimer models of full-length PP1α:R2 indeed confirmed that the IDoHA helix of R2 precludes the interaction of the C-terminal tail of PP1 with its catalytic core (Fig. 5c and Supplementary Fig. 5d).

To validate these in silico results experimentally, we designed a NanoBRET (Nanoluciferase Bioluminescence Resonance Energy Transfer) sensor that reports on the position of the C-terminus relative to the active site (Fig. 5d, Supplementary Fig. 5e). The BRET signal of this sensor is dependent on the distance between the N-terminally fused NanoLuc donor and the C-terminally fused HaloTag618 acceptor. The N-terminus of PP1 serves as a proxy for the active site as they both have a fixed position at a relatively short distance from each other. Displacement of the C-terminus from the active site increases the distance between the N- and C-termini, resulting in a decrease of BRET signal. We validated this principle using the PP1-binding domain of ASPP1 (residues 867-1090), which sequesters the C-terminus of PP1 in an extended conformation, away from the N-terminus and active

https://doi.org/10.1038/s41467-024-54256-4

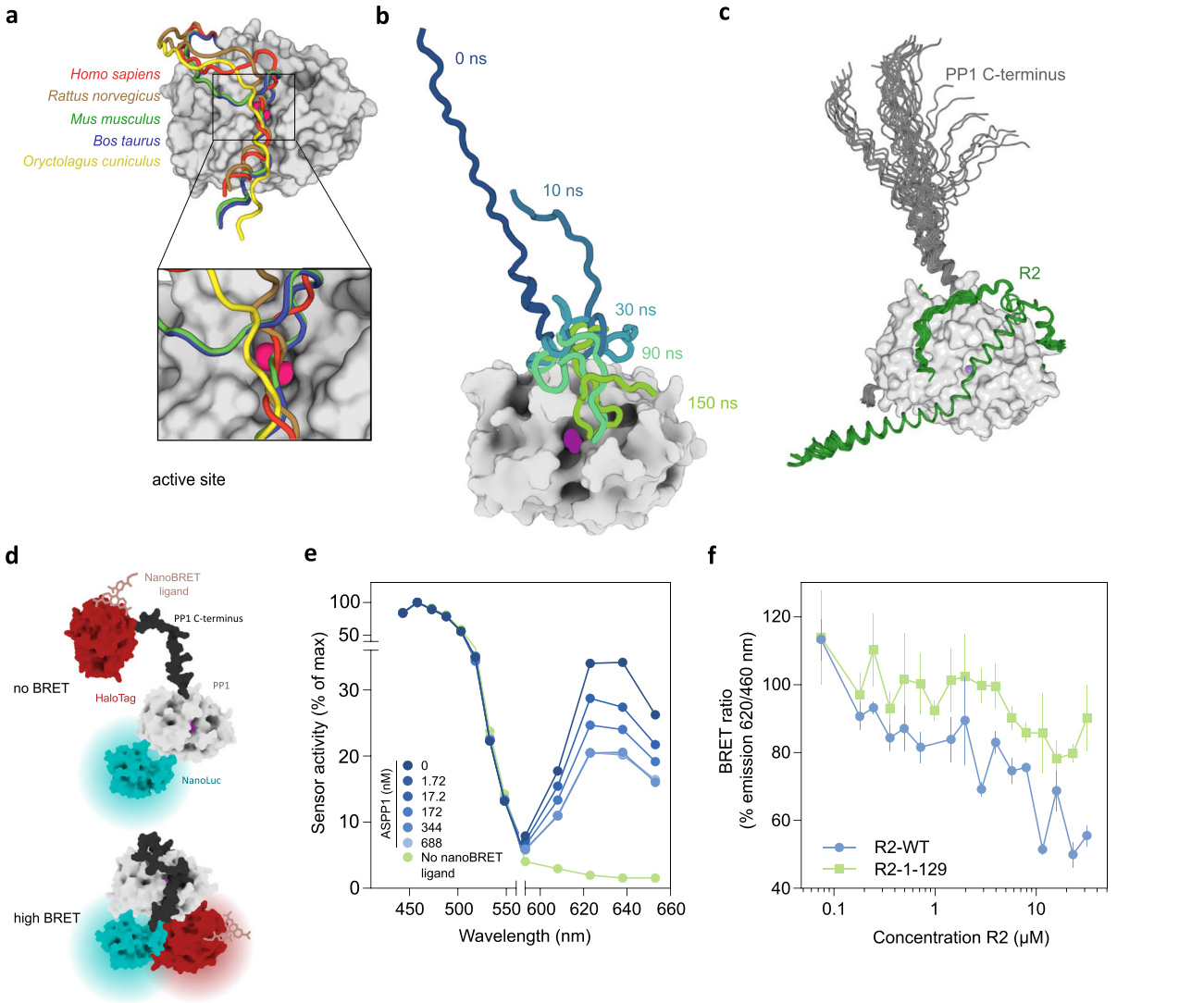

Fig. 5 | R2 disrupts the interaction between the C-terminus and catalytic domain of PP1. a Model of PP1α from the indicated species, as present in the AlphaFold Structural Database (EMBL-EBI), shows docking of the C-terminal tail in the acidic and hydrophobic grooves, thereby occluding the active site. The catalytic-site metals are shown as purple spheres in the enlarged inset. **b** Snapshots of the conformation of the C-terminal tail of PP1α during a 150-nanosecond all-atom molecular dynamics simulation of the catalytic subunit of PP1α. The catalytic domain of PP1α (residues 1–298) is represented as a gray surface, and the overlaid conformations of PP1 C-terminus (residues 299–330) at various intervals during the simulation in color. **c** Alignment of 50 AlphaFold-Multimer structural models of the complex between full-length PP1α and R2. The catalytic domain of PP1 is shown as a light-gray surface. The C-terminus of PP1 (dark gray) and R2 (green) are shown as ribbons for each individual model and are superimposed on the structure of human PP1α (PDB: 4MOV). Residues with low confidence scores (pLDDT <35) are not shown. **d** Illustration of the principle behind the nanoBRET sensor used to measure the average distance between the N- and C-termini of PP1, and to differentiate between a C-terminus that is unbound (low BRET) or docked at the active site (high BRET). **e** Full-spectrum measurement of the PP1-BRET sensor upon addition of the indicated concentrations of HIS-ASPP1-(867–1090). The luminescence spectrum of an unlabeled sensor lacking the NanoBRET 618 ligand is shown to indicate the baseline. In the presence of NanoBRET 618 (labeled sensor), the sensor activity is revealed. Also shown is the loss of BRET signal after addition of the indicated concentration of HIS-ASPP1-(867–1090), an established interactor of the C-terminal tail of PP1. **f** Dose-response curve showing the BRET signal upon addition of increasing concentrations of HIS-R2-WT or HIS-R2-(1–129). The results are depicted as means ± SEM of 6 technical replicates from 2 independent experiments.

site[7,34]. Accordingly, addition of purified HIS-ASPP1-(867–1090) decreased the BRET signal in a dose-dependent manner (Fig. 5e), confirming that the sensor reports on the position of the C-terminus. The addition of purified R2-WT also decreased the BRET signal in a dose-dependent manner (Fig. 5f), in agreement with an R2-induced displacement of the C-terminus of PP1 from the active site. This displacement was dependent on the IDoHA helix, as indicated by the less pronounced reduction of the BRET-signal by addition of R2-(1-129), which lacks the IDoHA helix that includes the HYNE sequence (Fig. 3a). In conclusion, both our in silico and in vitro approaches indicated that the C-terminus of PP1 dynamically interacts with the catalytic domain of PP1, and is displaced by the recruitment of R2.

Effects of R2 on the activity regulation of PP1 by its C-terminal tail

To explore the functional consequence of the displacement of the C-terminal tail of PP1 by R2, we first explored how the activity of PP1 is affected by its C-terminus. The C-terminal tail of PP1 (residues 299–330 of human PP1α) is conserved from yeast to man (Fig. 6a). Most conserved is a heptapeptide sequence, RPITPPR for human PP1α, which is hydrogen-bonded to the catalytic domain in molecular dynamics simulations (Supplementary Fig. 5c). We will further refer to this sequence as the PR-motif. To delineate the contribution of the C-terminus to the activity regulation of PP1, we first performed phosphatase-activity assays with 4 bacterially expressed and purified

https://doi.org/10.1038/s41467-024-54256-4

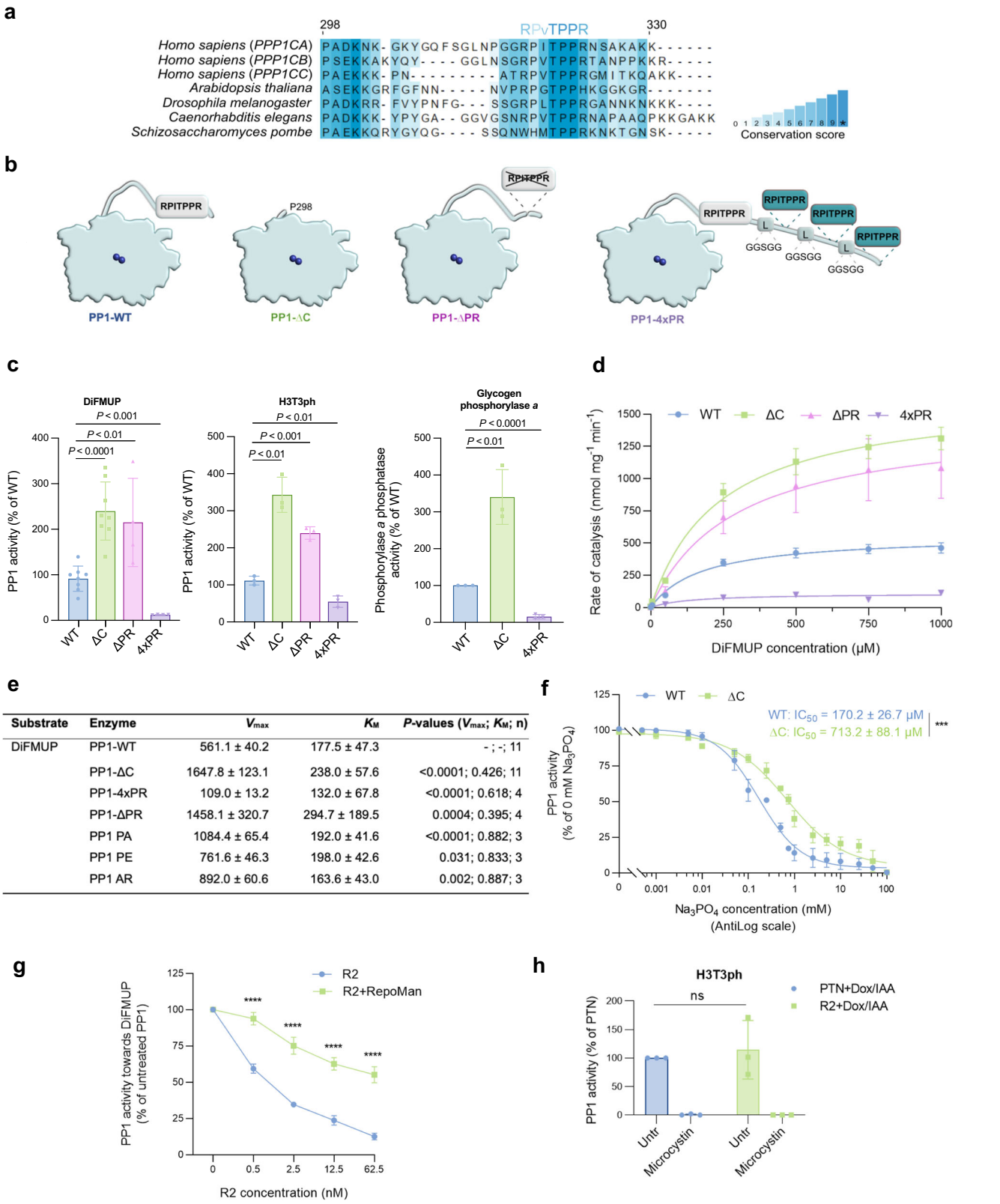

Substrate	Enzyme	V_{max}	K_M	*P*-values (V_{max}; K_M; n)
DiFMUP	PP1-WT	561.1 ± 40.2	177.5 ± 47.3	- ; -; 11
	PP1-ΔC	1647.8 ± 123.1	238.0 ± 57.6	<0.0001; 0.426; 11
	PP1-4xPR	109.0 ± 13.2	132.0 ± 67.8	<0.0001; 0.618; 4
	PP1-ΔPR	1458.1 ± 320.7	294.7 ± 189.5	0.0004; 0.395; 4
	PP1 PA	1084.4 ± 65.4	192.0 ± 41.6	<0.0001; 0.882; 3
	PP1 PE	761.6 ± 46.3	198.0 ± 42.6	0.031; 0.833; 3
	PP1 AR	892.0 ± 60.6	163.6 ± 43.0	0.002; 0.887; 3

GST-tagged variants of human PP1α (Fig. 6b and Supplementary Fig. 6a). These PP1 variants were wildtype PP1 (PP1-WT), PP1 lacking the C-terminal residues 299–330 (PP1-ΔC), PP1 with a deleted PR-motif (PP1-ΔPR) and PP1 with a C-terminus that has three additional PR-motifs, separated by flexible GGSGG-linkers (PP1-4xPR). The purified fusions were assayed with 3 different substrates, i.e. a small-molecule substrate that only contacts the active site (DiFMUP), a peptide substrate (residues 1–10 of histone H3, phosphorylated at Thr3; H3T3ph) and a protein substrate (glycogen phosphorylase *a*). With all substrates, the phosphatase activity was increased severalfold by deletion of the C-terminus (PP1-ΔC), and decreased up to 80% by addition of 3 extra PR-motifs (PP1-4PR) (Fig. 6c). The selective deletion of the PR-motif (PP1-ΔPR) increased the activity to a similar extent as deletion of the entire C-terminus. These data demonstrated that the

Fig. 6 | Inhibition of PP1 by its C-terminal tail. a Multiple protein-sequence alignment of the PP1 C-terminus. The sequences were obtained from unifrop.org: *H. sapiens*, P62136 (PP1CA), P62140 (PP1CB) and P36873 (PP1CC), *A. thaliana*, A0A178V1Q1; *D. melanogaster*, A0A0B4KHS9; *C. elegans*, P48727 and *S. pombe*, P13681. Sequences were aligned with ClustelOmega. Jalview (v2.11.3.2) was used to generate the conservation code. **b** Cartoons of the generated PP1α variants. **c** Phosphatase activities of GST-tagged PP1α-WT, PP1α-ΔC, PP1α-ΔPR and PP1α −4xPR (1–1.25 nM), assayed with DiFMUP (750 μM), a histone H3 peptide (H3T3ph, 750 μM) and glycogen phosphorylase *a* (10 μM) as substrates. Results are shown as means ± SD. The dots represent independent assays. *P* values were from Student's unpaired two-tailed t-test. **d** GST-PP1α variants (1.25 nM) were assayed with DiFMUP. **e** V_{max} and K_M values were derived from kinetic curves, as shown in panel (**d**), using GraphPad Software. Values of V_{max} are nmol of Pi released (mg of protein)/min. K_M values are represented in μM. The data in panels (**d**) and (**e**) are represented as means ± SEM of independent assays (n is indicated in Fig. 6e). The *P*-values in panel (**e**) were obtained using Student's unpaired two-tailed t-test. **f** GST-tagged PP1α-WT and PP1α-ΔC were assayed with DiFMUP (750 μM) and the indicated concentrations of Na_3PO_4 (P_i). The curves were generated using a four-parameter logistic equation. IC_{50} values were compared using Student's unpaired two-tailed t-test (***, $P < 0.001$). Error bars and IC_{50} values are shown as means ± SD of 3 independent assays. **g** Effect of RepoMan-(1–630) (50 nM) on the inhibition of GST-PP1α-WT (1 nM) by GST-R2. Results are represented as means ± SEM of 6 independent assays. ****, $P < 0.0001$ using Student's unpaired t-test. **h** Activity of PP1:RepoMan, immunoprecipitated from Dox/IAA-treated PTN and R2-degron cell lines and assayed with H3T3ph (100 μM), in the absence and presence of 1 μM microcystin. The results are expressed as a % of the activities in the parental cell line and shown as means ± SD of 3 biological repeats (n = 3). A Student's unpaired two-tailed t-test did not show a significant difference in the absence of microcystin (ns).

PR-motif is inhibitory for PP1 in a substrate-independent manner. We also generated PP1α mutants where the PR-motif was relieved from conformational restraint by mutation of proline to alanine (PP1-AR), or from the ability to engage in hydrogen bonding by eliminating (PP1-PA) or reversing (PP1-PE) the charge of its arginine (Supplementary Fig. 6b, c). These mutants were also more active than PP1-WT, but less active than PP1-ΔC (Fig. 6e and Supplementary Fig. 6d), indicating that both charge and conformation of the PR-motif contribute to decreasing the catalytic efficiency of PP1. Kinetic studies with DiFMUP as substrate revealed that the activity differences of the tested PP1 variants solely stemmed from changes in the V_{max} (Fig. 6d, e, and Supplementary Fig. 6d). The absence of significant K_M effects showed that the C-terminus of PP1 does not interfere with the binding of substrates at the active site. Finally, comparison of BRET sensors with PP1-WT and PP1-ΔPR showed that the PP1-ΔPR sensor was less affected by ASPP1 addition (Supplementary Fig. 6e), indicating a reduced binding of its C-terminal tail to the active site under basal conditions, which is in agreement with the increased specific phosphatase activity of the PP1-ΔPR variant.

In principle, the C-terminal tail of PP1 can reduce the V_{max} by lowering the rate of substrate to product conversion or by impairing product release. There is no obvious mechanism for interference of the C-terminal tail with the rate of product formation by PP1, as the conformation of the catalytic core of PP1 is not affected by deletion of its C-terminus (compare PDB 6GOI and PDB 4MOV). We envisaged that the C-terminal tail may reduce the catalytic efficiency of PP1 by dynamically altering the charge of residues that coordinate the active-site metals or the incoming phosphate[2,3]. If so, the C-terminal tail is expected to affect the pH-activity profile of PP1. However, the pH-activity profiles of PP1-WT and PP1-ΔC were identical (Supplementary Fig. 6f), arguing against an effect of the C-terminal tail on the rate of product formation. To examine effects of the C-terminal tail on product release, we compared the sensitivity of PP1-WT and PP1-ΔC to inhibition by their product, P_i. Intriguingly, purified PP1 was nearly completely inhibited by physiological concentrations of P_i (0.5–1.5 mM), but the inhibitory potency was decreased about 3-fold by deletion of the C-terminus (Fig. 6f). These data are consistent with a role for the C-terminal tail in hampering the release of P_i from the active site.

R2 is a well-established inhibitor of purified PP1 (reviewed by Lemaire and Bollen[9]), demonstrating that the displacement of the C-terminal tail of PP1 by R2 does not result in its de-inhibition, likely because the PP1-inhibitory C-terminus is replaced by a PP1-inhibitory motif of R2. However, the inhibitory potency of R2 was reduced by the addition of RepoMan, and was then not inhibitory at all at stoichiometric concentrations of PP1 and R2 (Fig. 6g and Supplementary Fig. 6g). As expected, R2 was also a less potent inhibitor after mutation of its PP1-binding RVxF (SQKW → SAKA), SILK (GILK → GAAA), or HYNE (HYNE → AAAA) motifs, and in all conditions addition of RepoMan further reduced its inhibitory potency (Supplementary Fig. 6h–j). Consistent with a role for RepoMan in reducing the PP1-inhibitory potency of R2, the specific enzymatic activity of PP1:RepoMan, immunoprecipitated from the R2-degron cells, was not affected by the depletion of R2 (Fig. 6h).

R2 and the C-terminal tail of PP1 interact with a common set of RIPPOs

The previous data demonstrated that R2 is a positive regulator of PP1 holoenzymes (Figs. 2 and 3), including PP1:RepoMan, but does not increase the specific phosphatase activity of purified or immunoprecipitated PP1:RepoMan (Fig. 6g, h). This led us to wonder whether R2 promoted dephosphorylation by PP1:RepoMan in intact cells through stabilisation of subunit interactions, thereby opposing their competitive disruption by other RIPPOs. We envisaged that R2 stabilized PP1 holoenzymes by providing an additional interaction site for RIPPOs via the released C-terminal tail of PP1. To identify RIPPOs that interact with the C-terminal tail of PP1, we used mass spectrometry to map proteins that are differentially associated with EGFP-tagged and transiently expressed PP1-WT, PP1-ΔC, and PP1-4xPR (Supplementary Data 4). Many differentially associated proteins were RIPPOs and RIPPO-interacting proteins, which were all retained much better by PP1-4PR and PP1-WT than by PP1-ΔC, hinting at a contribution of the C-terminal tail of PP1 to their binding. These proteins included iASPP and ASPP2, which are already known to interact with the PR-motif of PP1 and, therefore, served as validation of the experiment[7]. We noted a striking overlap between the RIPPOs and RIPPO-interacting proteins associated with R2-mAID-mClover (Fig. 4b, c) and the C-terminal tail of PP1 (Fig. 7a, b, Supplementary Fig. 7a, b), including various components of the URI/PPP1R19 and PNUTS/PTW complexes. The differential interaction of PNUTS and URI with PP1-4PR and PP1-ΔC was confirmed in co-immunoprecipitation experiments (Fig. 7c). It is also worth noting that three proteins (UBL4A, GET4 and BAG6) were retained much better by PP1-ΔC and PP1-WT than by PP1-4PR (Fig. 7a, b, Supplementary Fig. 7a, b). These proteins form a ternary complex that interacts with the hydrophobic surface of (misfolded) polypeptides and targets them for proteolytic degradation[35,36]. In conclusion, the above data indicated that the RIPPOs that interact with R2 (Fig. 4b–d) and the C-terminal tail of PP1 (Fig. 7a–c) are strikingly similar, hinting at a common recruitment mechanism for these RIPPOs.

R2 stabilizes PP1:RIPPO complexes by extension of the RVxF-docking site

To delineate the contribution of R2 and the C-terminal tail of PP1 to the PP1:RepoMan interaction, we performed NanoBiT split-luciferase interaction assays with bacterially expressed and purified LgBiT-PP1α^{WT}, LgBiT-PP1α^{ΔC} and RepoMan-SmBiT (Fig. 8a, b, Supplementary Fig. 8a), following an adapted protocol[37,38]. For RepoMan, SmBiT, flanked by GSTSG flexible linkers, was inserted into an unstructured region of RepoMan that is directly C-terminal to its PP1-binding region and close to the LgBiT-tagged N-terminus of associated PP1

https://doi.org/10.1038/s41467-024-54256-4

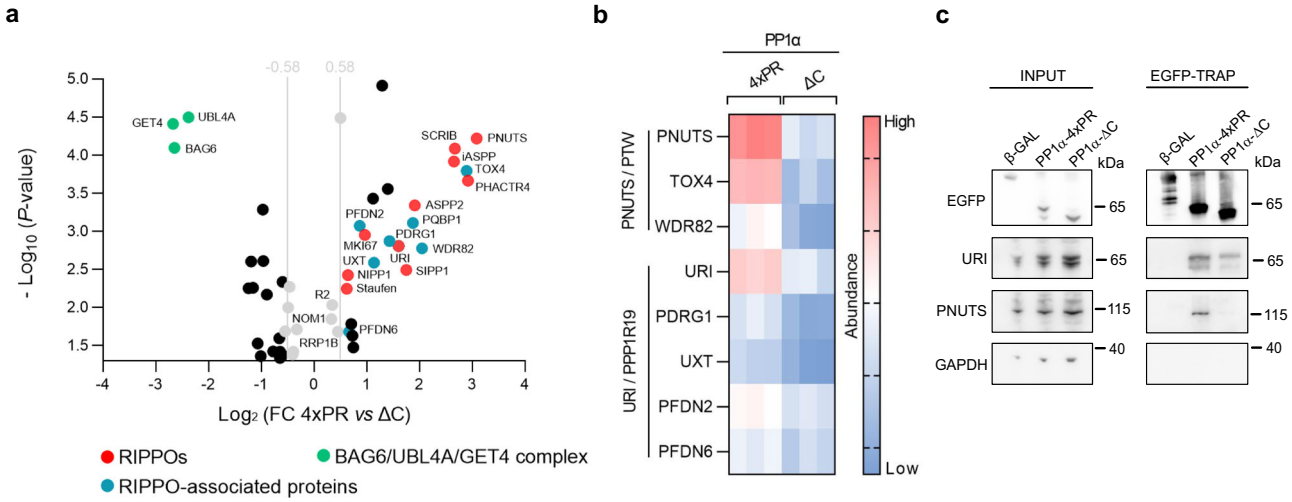

Fig. 7 | The interactome of the C-terminal tail of PP1a. a EGFP-tagged PP1α−4xPR or PP1α-ΔC mutants were transiently transfected in non-synchronized HEK293T cells, trapped from cell lysates after 24 h, and analysed by mass spectrometry. The panel shows a volcano plot for the differentially associated proteins. Each dot on the plot represents a polypeptide that exhibits a differential binding to PP1α−4xPR versus PP1α-ΔC. The plot is based on two parameters: fold-change (Log_2 of the fold-change (FC)) and statistical significance (Log_{10} of the *P*-value (threshold of $P < 0.05$)). The vertical gray lines indicate a fold change of 1.5. *P* values were determined using a 2-sided t-test of 3 biological repeats (n = 3). The corresponding *P*- and *Q*-values can be found in Supplementary Data 4. **b** Heatmap depicting the quantitative proteome differences in core proteins of the PNUTS/PTW and the URI/PPP1R19 complexes. Each condition is represented by 3 biological repeats (each lane represents 1 repeat). **c** HEK293 cells were transiently transfected with EGFP-tagged β-Galactosidase (β-GAL), PP1α−4xPR and PP1α-ΔC for 24 h. EGFP-traps of the lysates were immunoblotted for EGFP, URI and PNUTS. GAPDH served as loading control, immunoblotted in the same gel as for the EGFP (uncropped blots can be found in the Source Data). Shown immunoblots are representative of 3 (PNUTS immunoblot) or 2 (URI immunoblot) biological repeats.

(PDB:5IOH)[38]. Mixing of purified LgBiT-PP1α^{WT} and RepoMan-SmBiT resulted in a gradual rise in luciferase activity, reflecting holoenzyme assembly (Fig. 8c). As RepoMan has an RVxF-motif that is essential for PP1 binding[39,40], the assembled PP1:RepoMan complex could be disrupted by a molar excess of untagged RVxF-competing peptide, derived from NIPP1. A complex formed with PP1 lacking its C-terminus (LgBiT-PP1$^{\Delta C}$) was disrupted faster and at lower concentrations of RVxF peptide, consistent with a RepoMan contact site in the C-terminal tail that enhances its affinity for PP1. To delineate the contribution of R2, we generated the trimeric LgBiT-PP1:R2:RepoMan-SmBiT complex by including purified untagged R2^{WT} during sensor assembly. R2^{WT} diminished the competitive disruption by RVxF peptide in a dose-dependent manner (Fig. 8d). Importantly, stabilization by R2 was retained in a sensor lacking the C-terminal tail of PP1, indicating that R2 and the C-terminal tail stabilize the interaction between PP1 and RepoMan independently (Fig. 8e). To investigate the underlying mechanism, we modeled the structure of the R2:PP1:RepoMan-(341-450) complex, using AlphaFold V2-Multimer (Fig. 8f and Supplementary Fig. 8c, d). An ensemble of 75 models was generated, which were all in full agreement with the resolved regions from PP1:R2 and PP1:RepoMan crystal structures (2O8A and 5INB). However, upon analysis of the 15 top-ranked models, a deviation from the crystal structure was observed that involves the RVxF motif of R2 and its C-terminal flanking region (residues 48–70) (Fig. 8f), which were bound at the intersection between PP1 and two PP1-binding SLiMs of RepoMan, i.e. its RVxF and ΦΦ motifs[41]. R2 and RepoMan diverge at the base of the C-terminal tail of PP1, where they engage in contacts with a conserved lysine-rich region of the C-terminal tail (residues 301-305). The residues of R2 and RepoMan that were predicted to make contacts with PP1 or with each other are phylogenetically conserved (Supplementary Fig. 8b), indicating that their interaction serves an important function. We also produced Alphafold models for PP1:R2 bound to PNUTS, which was also identified as a common interactor of R2 and the C-terminal tail of PP1 (Fig. 4b–d, Fig. 7a, b). In the model of PP1:R2:PNUTS, we observed an assembly between the C-terminal tail of PP1, R2 and PNUTS that is similar to that of PP1:R2:RepoMan (Supplementary Fig. 8e, f). In contrast, when we modeled the PP1:R2:NIPP1 complex, no contacts between NIPP1 and R2 or the C-terminal tail of PP1 were observed, and key interactions of the central domain of NIPP1 with the catalytic domain of PP1 were disrupted (Supplementary Fig. 8g, h). These results are in line with our data showing that NIPP1 is not associated with R2 (Figs. 4b, 7a).

To validate the AlphaFold model, we made an R2 construct where the region (residues 48-70), predicted to make contacts with RepoMan and the C-terminal tail of PP1, was removed. Importantly, the deletion mutant still contained all its PP1-interacting sequences that are observed in crystal structures of PP1:R2 (PDB 2O8A, 2O8G), including the RVxF-motif (residues 44-47). In accordance with our structural model (Fig. 8f), deletion of this region from R2 eliminated its ability to enhance the binding between PP1 and RepoMan (Fig. 8d, e). Finally, we also validated the above data with trapping experiments of transiently expressed EGFP-tagged PP1α^{WT} or PP1α$^{\Delta C}$ in HCT116-WT and R2-HYNEm knock-in cells. RepoMan was much less associated with EGFP-PP1α following deletion of the C-terminal tail or expression of a PP1-binding mutant of R2 (R2-HYNEm), confirming that both R2 and the C-terminal tail of PP1 contribute to the stabilisation of the PP1:RepoMan complex (Fig. 8g).

Discussion

A coherent model of the biological function of PPP1R2 has not yet emerged, despite extensive research by multiple research groups for nearly 5 decades (reviewed by Lemaire and Bollen[9]). Depending on the adopted research models, R2 was identified as an inhibitor, activator or (metal) chaperone of PP1, or else as an allosteric regulator of Aurora A and Pin1. Here, using R2-degron and R2-HYNEm knock-in cell lines, we found that R2 regulates nuclear processes that contribute to cell proliferation by a mechanism that critically depends on its direct interaction with PP1 (Figs. 1–3). These data argue against an allosteric regulation of Aurora A and Pin1 as the primary function of R2[23,24]. The depletion or functional inactivation of R2 caused the hyper-phosphorylation of some but not all PP1 substrates (Figs. 2 and 3), indicating that R2 stimulates a subset of PP1 holoenzymes.

https://doi.org/10.1038/s41467-024-54256-4

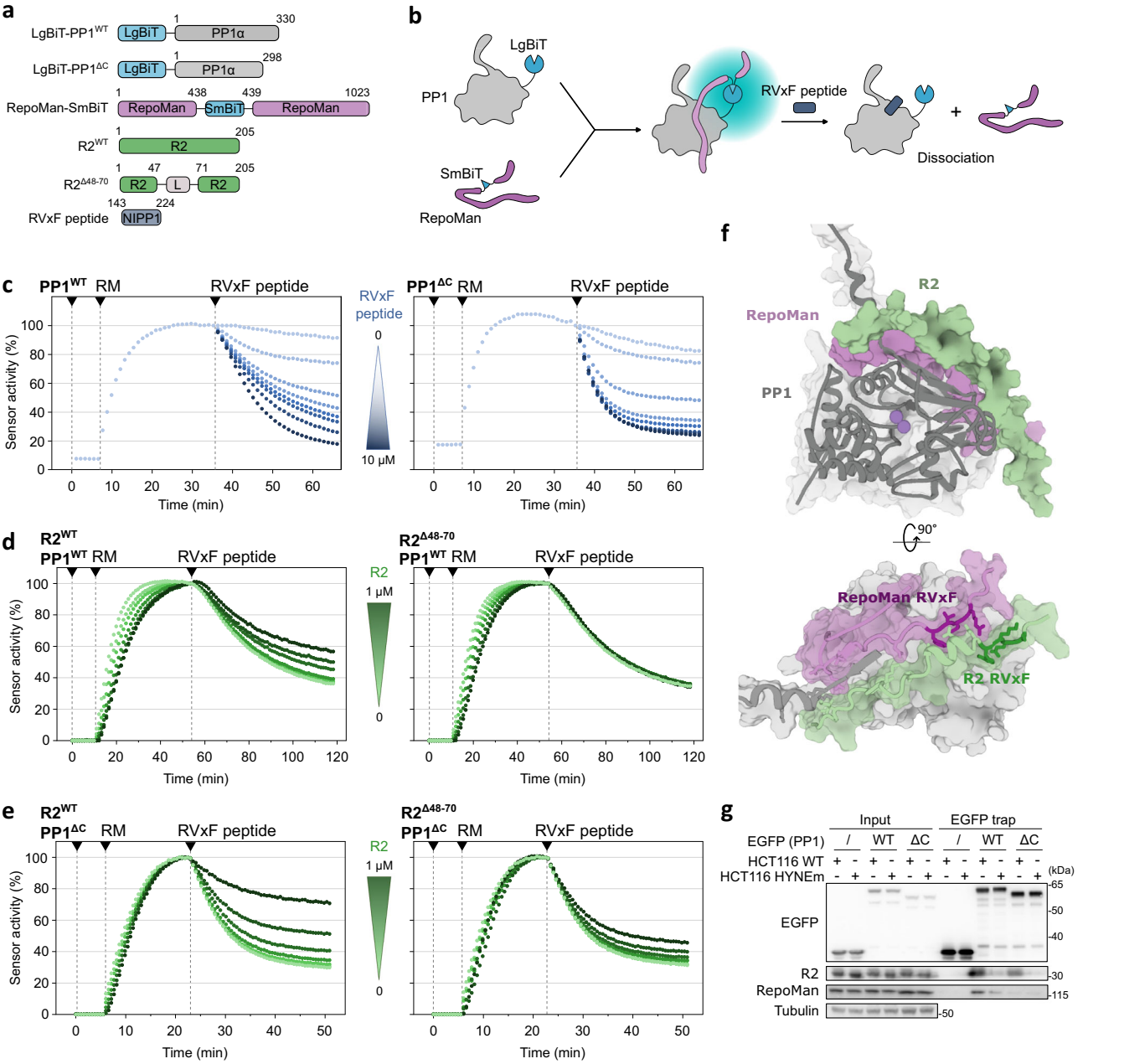

Fig. 8 | Stabilisation of PP1:RepoMan by R2. a Diagrams of the recombinant split-luciferase constructs and competitor proteins used in panels (**c**–**e**). L = 24-resisue flexible GS linker. **b** Cartoon representation of the principle of split-luciferase assays shown in panels (**c**–**e**). **c** Kinetic-trace experiments showing the gradual association of the LgBit-PP1$^{WT/\Delta C}$:RepoMan-SmBit sensors and their dissociation by addition of varying concentrations of RVxF competitor (NIPP1-(143-224) (0.64, 3.2, 16, 80, 400, 2000 or 10,000 nM). Data is plotted as the average of 2 technical repeats and normalized to the timepoint directly before competitor addition. For the association phase, only the control condition is plotted. **d** Kinetic-trace experiments showing the gradual association of LgBit-PP1^{WT}:RepoMan-SmBit in the presence of varying concentrations of untagged R2^{WT} or R2$^{\Delta 48\text{-}70}$ (0.32, 1.6, 8, 40, 200 or 1000 nM), followed by dissociation with a fixed concentration of RVxF peptide (1 µM). Data is plotted as in (**c**). **e** Same as (**d**) but for LgBit-PP1$^{\Delta C}$:RepoMan-SmBit. **f** Structural model of PP1α:R2:RepoMan-(341-450), generated by AlphaFold-multimer. The regions of R2 and RepoMan that are predicted to make direct contacts with each other and with the C-terminal tail of PP1 are depicted as green and pink cartoons, respectively. The RVxF-motifs of both proteins are highlighted. **g** EGFP-tagged PP1-WT and PP1-ΔC were transiently (48 h) expressed in HCT116 parental cells or R2-HYNEm knock-in cells. EGFP traps were probed for EGFP, R2 and RepoMan. Tubulin served as loading control.

Accordingly, we found that R2 stabilizes the interaction of some RIPPOs with PP1 by providing an additional, composite RIPPO-interaction site that extends the RVxF-docking site and is formed by an RVxF-flanking sequence of R2 and the C-terminal tail of PP1 (Figs. 7 and 8). Our findings indicate that only a subset of RIPPOs, including RepoMan, have an RVxF motif followed by complementary residues that can dock into this site, rendering them more resistant to competitive dissociation by RIPPOs that lack these complementary residues (Fig. 9). Hence, R2 increases the level of a subset of PP1:RIPPO complexes by strengthening their subunit interactions. The stabilisation of PP1 holoenzymes by R2 is reminiscent of the regulation of the SDS22:PP1:Inhibitor-3 complex, which is stabilized by simultaneous interactions of PP1 with both SDS22 and Inhibitor-3, as well as by a direct SDS22:Inhibitor-3 interaction[42]. Our work disclosed an unexpected resemblance between the regulation of PP1 and PP2A holoenzymes by their C-termini. Indeed, the stabilisation of ternary PP2A

https://doi.org/10.1038/s41467-024-54256-4

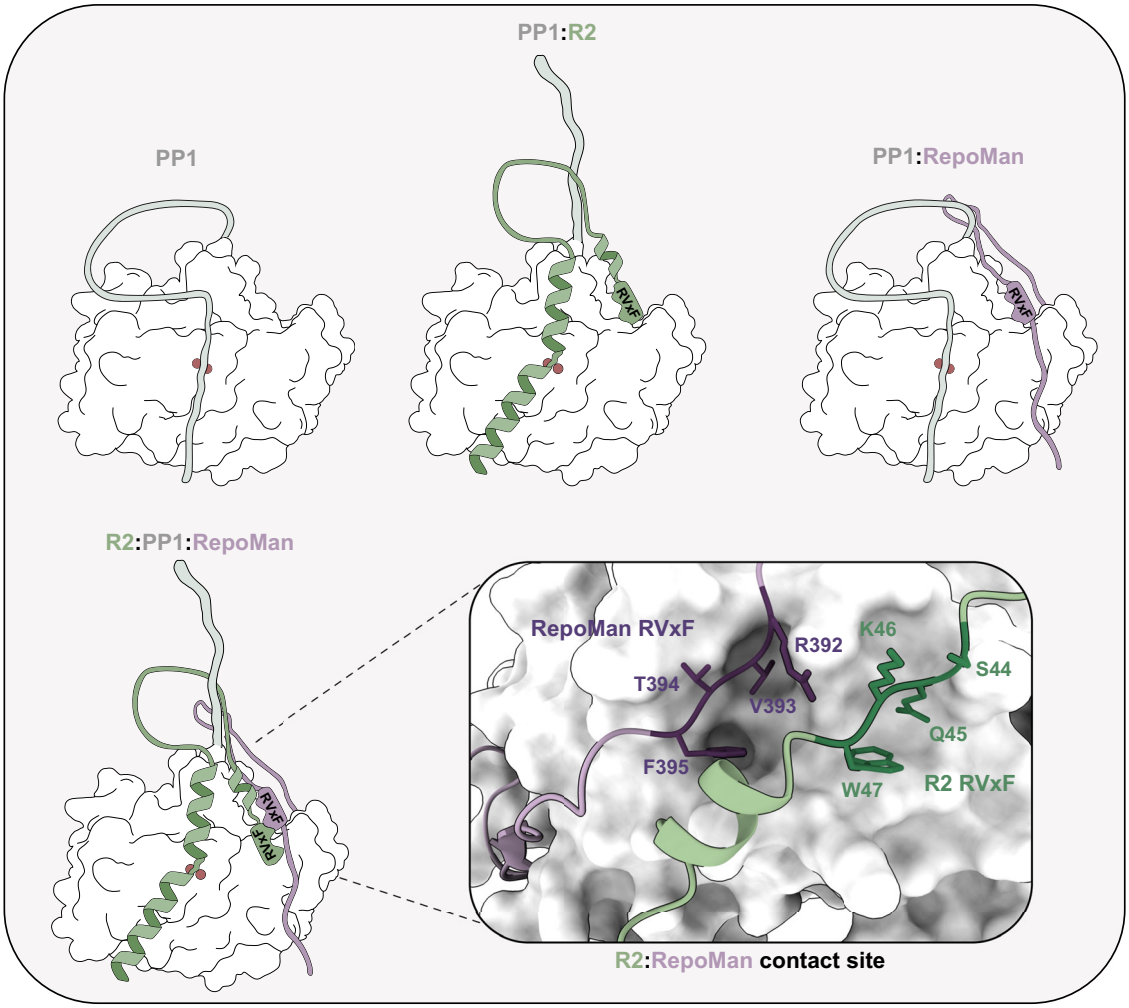

Fig. 9 | Model of the regulation of PP1 (holoenzymes) by PPP1R2. The figure shows models of PP1, PP1:R2, PP1:RepoMan and R2:PP1:RepoMan, based on available crystal structures and the data reported in this study. The C-terminal tail of PP1 is inhibitory because it dynamically docks to the active site (Fig. 5). R2 recruitment releases the C-terminal tail from the active site due to competition for an overlapping docking site on the catalytic domain. RepoMan does not interfere with the docking of the C-terminal tail of PP1. However, in the R2:PP1:RepoMan complex, the C-terminal tail of PP1 is displaced and associates with both R2 and RepoMan (Fig. 8). In addition, the degenerate RVxF motif of R2 is out-competed by the canonical RVxF motif of RepoMan, and RVxF-flanking residues of R2 directly interact with RepoMan. The additional, composite binding site for RepoMan created by R2 recruitment makes the complex resistant to dynamic exchange with RIPPOs that do not interact with R2.

complexes also involves the C-terminal tail of the catalytic subunit, which binds at the interface of A-type and B-type regulatory subunits[43–45], similar to the binding of the C-terminal tail of PP1 to both R2 and a subset of RIPPOs.

RepoMan forms a ternary complex with PP1 and R2 but does not have a structured domain that encapsulates the C-terminal tail of PP1, such as the ankyrin repeats of MYPT1 or the SH3 domain of ASPP proteins[6,7]. This indicates that RepoMan only interacts with a fragment of the C-terminal tail, as also suggested by our AlphaFold-multimer model (Fig. 8f). In addition, RepoMan also interacts directly with R2, thereby further stabilizing the R2:PP1:RepoMan complex (Fig. 9). It will be important to confirm our structural model of the interactions within the R2:PP1:RepoMan complex, using complementary experimental approaches for structural analysis, such as cryogenic electron microscopy or X-ray crystallography. The needed insights can clearly not be derived from the currently available, experimentally determined structures of the heterodimeric PP1:R2 and PP1:RepoMan complexes[12,41]. Indeed, R2 is not inhibitory for the ternary R2:PP1:RepoMan complex (Fig. 6g, h), arguing against occlusion of the active site by the IDoHA motif of R2 that is seen in the crystal structure of PP1:R2 (PDB: 2O8A)[12]. Also, our AlphaFold model suggests that the degenerate RVxF motif of R2 is displaced by the more canonical RVxF motif of RepoMan, and relocates adjacent to the RVxF-binding groove, where it interacts with residues of RepoMan (Figs. 8e and 9). It cannot be excluded that the ternary R2:PP1:RepoMan complex is additionally stabilized by fuzzy subunit interactions, which may only be revealed by tools of structure analysis that also detect dynamic interactions, such as NMR, or small-angle X-ray scattering in combination with size exclusion chromatography.

Our results are in accordance with many data in the R2 literature and provide a rationale for explaining seemingly contradictory findings. First, our results with the R2-degron and R2-HYNEm knock-in cell lines accord with R2 knockdown or knockout data, which also disclosed hyper-phosphorylation of a subset of PP1 substrates, all hinting at a PP1-stimulatory function of endogenous R2[21,22]. Second, our data confirm that R2 is an inhibitor of free PP1, but also revealed that R2 is not inhibitory for associated PP1:RIPPO complexes (Fig. 6g). Free PP1 does normally not accumulate in cells because of the large molar excess of RIPPOs, resulting in the rapid titration of free PP1[4]. Third, our findings shed light on why R2 is inhibitory to PP1 when it is overexpressed (see Lemaire and Bollen for references[9]). On the one hand, overexpressed R2 maximally stabilizes associated PP1 holoenzymes

(this work), resulting in the hypo-phosphorylation of a (small) subset of PP1 substrates. On the other hand, overexpressed R2 also competitively disrupts (most) other PP1 holoenzymes containing RIPPOs that do not interact with R2[46]. This likely results in the accumulation of inactive PP1:R2 heterodimers and the hyper-phosphorylation of most PP1 substrates. Fourth, DNA-damage causes ATM-mediated phosphorylation of R2 at Ser44, resulting in its dissociation from PP1[47]. Our data suggest that this phosphorylation may actually serve to prevent the stabilisation of PP1 holoenzymes that are important for cell proliferation, thereby contributing to DNA-damage induced cell-cycle arrest. Our studies on R2-degron and knock-in cell lines did not provide evidence for a role of R2 as a metal chaperone for PP1, as the specific enzymic activity of purified PP1 was not affected by prior R2 depletion. However, it cannot be excluded that a metal-loading function of R2 was masked in our experiments by functional redundancy with other RIPPO(s).

An unexpected finding of our study was that the V_{max} of PP1 is reduced severalfold by the PR-motif in its C-terminal tail, probably due to hampered P_i product release through dynamic occlusion of the active site (Fig. 6). In the context of PP1 holoenzymes, inhibition by the C-terminal tail may be alleviated by the recruitment of RIPPOs such as the MYPT and ASPP proteins. Remarkably, R2 did not increase the specific activity of associated PP1:RepoMan, despite the displacement of the C-terminal tail from the active site (Fig. 6). An enticing hypothesis is that R2-associated PP1:RepoMan can be further activated by an additional, hitherto unknown allosteric control mechanism involving, for example, a covalent modification of one of its subunits.

SDS22 and Inhibitor-3 are the first evolved RIPPOs. They both function as potent inhibitors of PP1 in vitro. However, in a cellular context SDS22 and Inhibitor-3 form a ternary complex with newly translated PP1, which is a substrate for p97/VCP-mediated transfer of PP1 to canonical RIPPOs, thereby forming functional PP1 holoenzymes[42,48]. PPP1R2 is the third evolved RIPPO and is also a potent inhibitor of PP1 in vitro. Here, we demonstrated that R2 is not inhibitory for associated PP1 holoenzymes and actually enhances the dephosphorylation of their substrates through stabilization of subunit interactions, culminating in higher holoenzyme levels.

Targeting PP1 holoenzymes has a significant therapeutic potential[49,50], but is highly challenging due to a lack of specific PP1:RIPPO interaction sites[51]. For example, targeting the RVxF-docking site interferes with a majority of PP1 holoenzymes and, therefore, affects numerous cellular processes. In contrast, the composite R2:PP1:RIPPO interaction site described here is more unique and seems druggable, as it constitutes a deeply buried groove suited for the docking of small-molecule, drug-like compounds. More generally, our study illustrates the importance of exploring (dynamic) subunit interactions to elucidate the intricacies and multifaceted nature of PP1 regulation, which has implications for the development of PP1 holoenzymes as therapeutic targets.

Methods

Materials

The sequences of all new constructs generated for this study are shown in Supplementary Data 5. The source of all key materials (chemicals, constructs, antibodies, cell lines) and used software is provided in Supplementary data 6.

Protein expression and purification

Constructs for His- and GST-tagged proteins were cloned into the pET16b or pGEX-2TK vector, respectively, and expressed in BL21 gold cells at 37 °C in LB medium with 100 μg/ml ampicillin. The cells were grown until an OD600 of ≈ 0.6, when protein expression was induced for 20 h at 18 °C with 1 mM isopropyl β-D-1-thiogalactopyranoside (IPTG). Cell pellets with His-tagged proteins were lysed with 10 volumes of a buffer containing 20 mM Tris at pH 7.9, 0.5 M NaCl, 5 mM imidazole, 0,5% Triton X-100, 0.5 mg/ml lysozyme and a cocktail of protease inhibitors (1 mM PMSF, 1 mM benzamidine, 5 ug/ml leupeptin). For the extraction of PPP1R2 variants, the cells were lysed in 6 M urea, supplemented with 0.5 M NaCl, 0.5% Triton X-100 and the same cocktail of protease inhibitors. Cell lysis was completed with one freeze-thawing cycle. Cells expressing GST-tagged proteins were lysed in 10 volumes of a buffer containing 50 mM Tris at pH 7.5, 0.3 M NaCl, 1 mM DTT, 0.5% Triton X-100, 1 mM $MnCl_2$, 0.5 mg/ml lysozyme and protease inhibitors (0.5 mM PMSF, 0.5 mM benzamidine, 5 ug/ml leupeptin). Lysates containing His-tagged proteins were cleared by centrifugation (20 min at 15,000 x *g*) and the supernatant was loaded for 1 h at 4 °C onto HisPur™ Ni-NTA agarose. The Ni-NTA agarose beads were first washed with 20 volumes of a buffer containing 20 mM Tris at pH 7.9, 0.5 M NaCl, 50 mM imidazole, and then eluted with 20 mM Tris at pH 7.9, 0.5 M NaCl, and 400 mM imidazole. The eluate was dialyzed overnight against 20 mM Tris at pH 7.4, 0.5 M NaCl, 1 mM DTT or 0.5 mM TCEP. Glutathione agarose, equilibrated with 50 mM Tris at pH 7.5, 0.15 M NaCl, 1 mM DTT, 1 mM $MnCl_2$, 0.5 mM PMSF and 0.5 mM benzamidine, was used for the purification of GST-PP1 variants (Fig. 6c, d, f, g and Supplementary Fig. 6a–j). The loaded glutathione-agarose beads were first washed, as described above, and eluted with four column volumes of 0.1 M Tris at pH 8.0, 1 mM DTT, 1 mM MnCl2 and 10 mM reduced glutathione. The eluted fractions with a GST-tagged protein were pooled and dialyzed overnight at 4 °C against 50 mM Tris at pH 7.5, 0.1 M NaCl, 1 mM DTT and 60% glycerol, and stored at −80 °C. GST-R2 was purified like GST-PP1α, but in the absence of $MnCl_2$.

The partial purification of PP1 from HCT116 parental and R2-degron cells to a stage that it was free from contaminating phosphatases and RIPPOs, was based on a published protocol[28]. First, the cells were lysed with modified RIPA buffer (20 mM Tris at pH7,5, 150 mM NaCl, 1 mM EDTA, 1 mM EGTA, 1% NP40, 1% sodium deoxycholate). Subsequently, proteins were precipitated by the gradual addition of ammonium sulfate (313 g/liter) to the stirring lysates. After 30 min, the precipitated proteins were collected by centrifugation (30 min at 30,000 x *g*). The pellet was resuspended in 20 mM Tris at pH 7.5, 10% glycerol, 1 mM PMSF and 1 mM DTT, and supplemented with 5 volumes of 95% ethanol. The precipitated proteins were collected by centrifugation for 5 min at 30,000 x *g*. The pellet was resuspended in 20 mM Tris at pH 7.5, 1 mM PMSF and 1 mM DTT, and cleared by centrifugation (5 min at 30,000 x *g*). The supernatant was loaded onto a column of heparin Sepharose. The column was washed with 20 mM Tris at pH 7.5, 1 mM DTT and 0.1 M NaCl, and subsequently eluted with the same buffer but with 0.5 M of NaCl. The eluate was dialyzed overnight against 20 mM Tris at pH 7, 1 mM DTT and 10% glycerol, and stored at −80 °C.

Generation and treatment of cell lines

The R2-degron cell line was generated as detailed by Cao et al.[42]. A guide RNA directed the Cas9 protein to a PAM site at the 5′-end of the stop codon of the R2-encoding *PPP1R2* alleles (Fig. 1a). The templates for recombination-mediated repair of Cas9-induced double-strand breaks had homology arms bordering consecutively a miniature Auxin-Inducible Degron (mAID), a mClover-encoding cassette, and a neomycin- or hygromycin-resistance cassette. The modified *PPP1R2* alleles encoded R2 with a C-terminal mAID-mClover tag. The HCT116 parental and R2-degron cell lines contained a transgene at the AAVS1 locus that expresses the F-box protein TIR1 from *Oryza sativa* in a doxycycline (Dox)-dependent manner. Addition of Dox to induce the expression of TIR1 and IAA (Indol-3-Acetic Acid, a synthetic analog of auxin) to recruit the endogenous SCF-type E3 ubiquitin ligase to mAID leads to the ubiquitination and proteasomal degradation of R2-mAID-mClover in the R2-degron cell line. The degradation of R2 in the HCT116 degron cell lines was induced with 2 μg/ml Dox and 500 μM IAA. Unless indicated otherwise, the drug treatment was for 48 h.

HCT116 knock-in cell lines were purchased from Synthego Corporation (Redwood City, CA, US). In these cell lines, both alleles of *PPP1R2* were mutated (^{147}HYNE^{150} → AAAA, HYNEm), using CRISPR/Cas9. AGGAAGCUUCACUACAAUGA was used as guide RNA (guide RNA cut location chr3:195,519,142). The PCR and sequencing primers were AGGCATAGACCATTACAAAAGTCT (5′→3′; forward primer) and TGGCTGGATATATTCTTGTTCTTCCA (5′→3′; reverse primer). The donor sequence for generating the R2-HYNEm cell lines was CTTTTGAAATTAATTGTCTGGCTAGTTTGATATTGAGTCCTGCAGCTG CAGCAAGCTTTCTTTTCATTTCAAATTGTCGCTTTTTTTCTAT. Single-cell dilution was used for clonal isolation. The isolated clones were verified by Sanger sequencing.

The R2-degron and knock-in cell lines were cultured at 37 °C with 5% CO_2. HCT116 parental and R2-degron cell lines were cultured in low-glucose DMEM, while HCT116 parental and R2-knock-in cell lines were cultured in McCoy's 5 A medium. HEK293T cells were cultured in high-glucose DMEM. All cell-culture media were supplemented with 10% fetal calf serum, 100 units/ml penicillin and 100 μg/ml streptomycin. Transfections were done with JetPrime transfection reagent, according to manufacturer's instructions.

For IncuCyte live-cell assays, cells were plated in a 96-well plate at 6–8 ×10^3 cells per well. Confluency of the cultures was measured every 3 h using an IncuCyte S3 (Sartorius). For Sulforhodamine B (SRB) fluorogenic assays, cells were plated in a 96-well plate at 2 ×10^3 cells per well. At the indicated time points, cells were fixed with 10% trichloroacetic acid and stained for 30 min with SRB dye. Excess of dye was removed by washing with 1% acetic acid. Plates were dried and the remaining dye was solubilized in a 10 mM Tris-base solution. The OD was measured at 450 nm using a Tecan Spark plate reader. A prometaphase arrest was induced by consecutive treatments with 2 mM thymidine for 24 h, thymidine washout for 3 h and incubation with 100 ng/ml nocodazole for 15 h. A G_1/S-arrest was induced by a double thymidine arrest, involving consecutively a treatment for 18 h with 2 mM thymidine, a thymidine washout for 9 h, and a treatment for 15 h with 2 mM thymidine. To analyse mitotic phosphoproteins by immunoblotting, cells were synchronized at the G_2/M transition by a consecutive treatment with 2 mM thymidine for 24 h, a thymidine washout for 3 h, and incubation with 9 μM RO3306 for 15 h. The cells were released for the indicated time points (Figs. 2e, 3f and Supplementary Fig. 2g). For cell-cycle analysis with flow cytometry, cells were harvested by trypsinization, washed with PBS and fixed overnight with 70% ethanol at −20 °C. The cells were washed twice with PBS, resuspended in PBS with 0.05% Triton X-100 and 0.1 mg/ml RNAse A, and incubated for 30 min at 37 °C. Propidium iodide was added to a final concentration of 70 μg/ml. Analysis was performed using a BD Canto II and quantification using FlowJo software. Single cells were gated by plotting propidium iodide (PI) fluorescence signal height (PI-H) against PI fluorescence signal area (PI-A), allowing for the exclusion of cell doublets and aggregates. Cells falling along the diagonal line of the PI-H versus PI-A plot were selected for further analysis, ensuring a population of singlets. The gating strategy used for flow cytometry analysis is shown in Supplementary Fig 1f. For live cell imaging, the Leica TCS SPE laser-scanning confocal microscope was used with a live-imaging chamber (37 °C and 5% CO_2) and a monochrome digital camera DFC365 FX from Leica. For time-lapse imaging, cells were grown in a 24-well plate.

Phosphatase-activity assays

In vitro phosphatase activity assays with the fluorogenic 6,8-difluoro-4-methylumbelliferyl phosphate (DiFMUP) substrate were conducted at 30 °C in 384-well plates in a final volume of 40–50 μl and at a final substrate concentration of 0.5 μM − 1000 μM, as indicated in the corresponding figure legends. The assay buffer contained 50 mM Tris at pH 7.4, 100–150 mM NaCl, 1-5 mM DTT, 0.1–1 mg/ml BSA and 0.05% Tween 20. The pH-activity profiles of GST-PP1α variants were obtained in an assay buffer containing 20 mM Tris, 20 mM acetic acid, 20 mM HEPES, 100 mM NaCl, 5 mM DTT, 1 mg/ml BSA and 0.05% Tween 20, and the pH was adjusted with HCl or NaOH, to obtain a pH range from 4.0–12.0. Phosphatase activities were measured at 30 °C within a timeframe ranging from 7–10 cycles of 3–5 min each, on a Tecan Spark® reader at an excitation of 358 nm and emission of 455 nm. The GST-PP1 variants were assayed at a concentration of 0.5–1.25 nM, as specified in the Fig. legends. GST-R2 (FL) and His-RepoMan-(1-630) were used at a concentration of 0.5–62.5 nM and 50 nM, respectively.

Phosphatase activity assays with H3T3ph peptide (AR-pT-KQTARKS) as substrate was performed with the colorimetric BIOMOL® Green assay kit, and phosphate production was measured at 650 nm with a Tecan Spark® reader. The reactions were performed in 384-well plates and started by incubation of the GST-PP1α variants with the H3T3ph peptide for 30 min at 30 °C in an assay buffer containing 30 mM Tris at pH 7.4, 100 mM NaCl, 1 mg/ml BSA, 1.5 mM DTT and 0.05% Tween 20. The final concentrations of recombinant PP1α and H3T3ph in the assay were 1.25 nM and 750 μM, respectively. The reaction was stopped by adding 40 μl BIOMOL® Green reagent to 20 μl of assay mixture. The absorbance was measured after 30 min incubation at room temperature. Phosphatase activity assays with radioactively labeled glycogen phosphorylase *a* as substrate were performed as previously described[29].

Immunoblotting and immunoprecipitation

Cells were lysed with a modified RIPA buffer (20 mM Tris at pH7,5, 150 mM NaCl, 1 mM EDTA, 1 mM EGTA, 1% NP40, 1% sodium deoxycholate), supplemented with protease inhibitors (1 mM PMSF, 1 mM benzamidine, 5 ug/ml leupeptin) and phosphatase inhibitors (50 mM NaF, 10 mM β-glycerophosphate, 1 mM vanadate). The lysates were cleared by centrifugation (10 min at 21,000 x *g*), yielding supernatant 1 (S1) and a pellet. The pellet was incubated for 30 min at 37 °C in the presence of micrococcal nuclease (300 units/ml, Thermo Scientific). After centrifugation for 10 min at 1500 × *g*, supernatant 2 (S2) was combined with S1, termed lysate, and the protein concentration was determined using the Bradford assay. For immunoprecipitation of endogenous proteins, the lysates were incubated with antibody for at least 3 h. Subsequently, Protein-A Sepharose beads were added for 1 h and the sedimented beads were washed with lysis buffer. SDS-PAGE was performed with 4–12% or 10% Bis-Tris gels and the separated proteins were transferred onto PVDF or nitrocellulose membranes for minimal 2 h at 40 V in 50 mM Tris and 50 mM boric acid. Subsequently, the membranes were blocked in 5% milk/TBS and 0.05% Tween20, or in 5% BSA/TBS-Tween20 when phospho-epitope specific antibodies were used. Primary antibodies were diluted in 5% milk/TBS-Tween20 or 5% BSA/TBS-Tween20 for phospho-epitope specific antibodies, and added overnight at 4 °C. Next, the membranes were washed twice with TBS-Tween20 and incubated for 1 h at room temperature with the HRP-coupled secondary antibody. Immunoblots were visualized using ECL reagent (PerkinElmer) in an ImageQuant LAS4000. Quantifications were performed with ImageQuant TL using rolling-ball background subtraction.

Trapping of EGFP-tagged β-Galactosidase, PP1α-WT, PP1α-ΔC and PP1α−4xPR for analysis of associated proteins (Fig. 7a–c) was performed as described[52]. In brief, asynchronized HEK293T cells were seeded in 15-cm plates and transfected for 24 h with 8 μg of plasmids. The cells were lysed for 20 min on ice with modified RIPA lysis buffer containing 50 mM Tris at pH 7.5, 300 mM NaCl, 1 mM EGTA, 1 mM EDTA, 1% NP-40 and 1% sodium deoxycholate, and supplemented with a cocktail of protease (cOmplete™ Protease Inhibitor Cocktail) and phosphatase (PhosSTOP™) inhibitors. 500 μl of lysate were cleared by centrifugation (10 min at 3000 x g) and incubated for 1 hour at 4 °C with 60 μl of nanobody EGFP beads (1:1 suspension). The beads were washed 3 times with Tris-buffered saline, supplemented with 0.1% Triton-X100 and 0.25% NP-40 and processed for proteomics analysis.

Immunostainings

For confocal-microscopy analysis, cells were seeded on polylysine-coated glass coverslips, fixed for 15 min at 37 °C in 4% formaldehyde, and washed with PBS. The cells were permeabilized in PBS for 5 min at room temperature with 0.5% of Triton X-100, and blocked for 30 min with 3% BSA (Sigma) in PBS. The permeabilized cells were incubated overnight at 4 °C with the primary antibodies, diluted in 3% BSA/PBS. Subsequently, the cells were incubated for 1 h at room temperature with secondary antibodies diluted in 3% BSA/PBS. DNA was stained with DAPI. Confocal images were acquired with a Leica TCS SPE laser-scanning confocal system mounted on a Leica DMI 4000B microscope and equipped with a Leica ACS APO 63×1.30NA oil DIC objective. All immunofluorescence images of similarly stained experiments were acquired with identical illumination settings. The brightness and contrast were adjusted using only linear operations applied to the entire image.

qPCR

Total RNA was isolated from cells using the GenElute™ Mammalian Total RNA Miniprep Kit from Sigma. Complementary DNA (cDNA) was synthesized from total RNA using oligo (dT) primers, RevertAid Premium Reverse Transcriptase and RiboLock RNase inhibitor enzymes. RT-qPCR reactions were performed using the Rotor-Gene Q instrument and the SYBR Green qPCR Mix (Invitrogen). Values were normalized against the housekeeping gene *HPRT*.

AlphaFold-Multimer modeling

The structural models of full-length PP1α from different species were retrieved from the AlphaFold Structural Database (EMBL-EBI) and were aligned to the crystal structure of PP1α (PDB: 4MOV). The structure of PP1α:PP1R2 was modeled using the AlphaFold-Multimer V2 pipeline that is implemented on the HPC-Ugent branch of the Flemish Supercomputing Center (VSC). The sequences of human PP1α, RepoMan (residues 341–450) and PPP1R2 were retrieved from Uniprot, and were submitted to the pipeline in two different chronological orders for PP1:R2 (PP1α:R2 and R2:PP1α) and three different orders for PP1:R2:RepoMan (R2:RepoMan:PP1; RepoMan:PP1:R2; PP1:R2:RepoMan). The multiple-sequence alignment was produced using the MMseqs2 protocol and the UniRef100 sequence database. For each submission, the multiple-sequence alignment was combined with 25 randomly-chosen seeds to produce 25 distinct structural models, for the PP1:R2:RepoMan model only the top five model of each submission were considered for evaluation. All models were energy-minimized using Amber, and were processed and visualized in PyMol. Regions of the structure that had low confidence (pLDDT <45) were omitted from the visualization of the structure.

Molecular-dynamics simulation

A structural model of PP1α with extended C-terminus was subjected to all-atom molecular dynamics simulation using the GROMACS package (GROMACS/2024.2-foss-2023b-CUDA-12.5.0)[53], installed on the HPC-Ugent branch of the Flemish Supercomputing Center (VSC). The system was built using the AMBER99SB-ILDN force field, which is well-suited for simulating the dynamics of protein sequences that are intrinsically disordered, to generate the essential topology records[54]. The simulation volume was defined as a cube where each face was distanced >1 nm from the surface of PP1α. Solvation was performed using the spc216 generic equilibrated 3-point solvent model. Four sodium ions were added to neutralize the net charge of the system. Inappropriate energy-minimization was performed to negate any inappropriate geometries, and was completed when the maximum force of the system dropped below 1000 kJ/mol/nm, at which point the system had a potential energy of $-6.87.10^6$ kJ/mol. The system was equilibrated to ambient conditions by performing a 100-picosecond isothermal-isochoric simulation at 298 K, followed by a 100-picosecond isothermal-isobaric simulation at 1 bar. The equilibrated system was used as the starting point for six 150-nanosecond production runs to evaluate the dynamics and binding behavior of the C-terminus of PP1α. The conformations of the C-terminus of one representative simulation were extracted at the indicated timeframes using Visual Molecular Dynamics (VMD) software (University of Illinois), and were overlaid with the crystal structure of PP1α (4MOV) in PyMol. The trajectory of all simulations was visualized and exported as a movie using PyMol. RMSF plots were generated by analysis of trajectories with the 'gmx rmsf' command, and hydrogen bonding behavior of the RPITPPR sequence was generated by analysis of trajectories with the 'gmx contact' command.

NanoBRET assays

The purified His-tagged NanoLuc-PP1α-HaloTag sensors (1 nM) was labeled with the NanoBRET 618 ligand (5 nM) in Tris-buffered saline for 30 min at room temperature, after which aliquots were flash-frozen and stored at −80 °C. Luminescence was measured in white 384-well non-binding plates on a Tecan Spark plate reader, using the luciferase substrate furimazine (25 μM). For assays, aliquots were thawed in water at room temperature and the luminescent spectrum of the sensor was recorded to confirm functionality of the sensor. For competition assays with purified ASPP1 or R2 (WT and 1–129 mutant), the BRET signal was quantified by making the ratio of the emission of the NanoBRET 618 ligand acceptor (595–700 nm) over that of the NanoLuc donor (445–470 nm) at ~30 °C. Data was plotted as a percentage of the BRET ratio of sensor treated with negative control. All assays were performed in parallel on an unlabeled control sensor to detect non-specific assay interference.

Split-luciferase assays

Split-luciferase assays were generally performed as described by Claes et al.[38]. All assays were executed in an assay buffer consisting of 50 mM HEPES at pH 7.4, 10% glycerol, 150 mM NaCl, 0.01% saponin, 0.005% Tween-20, 1 mM DTT, 0.5 mM EDTA and 5 μg/ml leupeptin. Split-luciferase components were purified from bacteria as described earlier. Assays were performed in white non-binding 384-well plates by dispensing 10 μl assay buffer solution containing 0.15 nM of $LgBiT^{WT/\Delta C}$-tagged sensor construct, the indicated amounts of His-R2 and 50 μM furimazine. To this mixture, 10 μl of SmBiT-RepoMan (0.025 nM to WT fusion or 0.1 nM to the ΔC fusion) were added. Competition with RVxF peptide was performed with the amounts indicated in the Fig. The plate was incubated and measured at room temperature at regular intervals (kinetic measurements) on a TecanSpark plate reader, using a PMT voltage of 900 mV and an integration time of 500 ms (Tecan, Mannedorf, Switzerland). Assay interference was mitigated by performing all assays in parallel on a control sensor, according to Claes et al.[38].

(Phospho-)proteomics

Traps (60 μl of EGFP beads) of EGFP-tagged PP1α-WT, PP1α-ΔC and PP1α−4xPR from lysates of asynchronous HEK293T cells (n = 3 biological repeats) were washed twice with 50 mM Tris HCl at pH 8.5, once with 50 mM ammonium bicarbonate (AMBIC), twice with 50 mM AMBIC containing 0.0025% ProteaseMAX, and subjected to unbiased interactomics as described by Cokelaere et al.[55]. Peptides were identified by Mascot (Matrix Science) through Proteome Discoverer (PD) 2.2 (Thermo Fisher) using the Uniprot Homo sapiens database. The database (204,906 entries) was compiled with reviewed (Swiss-Prot) and unreviewed (TrEMBL) hits obtained after filtering the complete UniProtKB for 'Homo sapiens' in the fields 'ALL' and 'TAXONOMY'), and was validated using the PD Percolator node ($q < 0.01$). Progenesis (Nonlinear Dynamics) was used for relative quantification of peptides and only unique peptides were considered. Proteins were considered

as PP1α interactors if their prevalence (= protein abundance divided by total feature abundance w/o bait) was significantly (2-sided t-test, $P < 0.05$) different in the PP1α-WT, PP1α−4xPR and PP1α-ΔC conditions versus the β-Galactosidase control condition. Proteins were considered to be differential interactors between different PP1α-WT, PP1α−4xPR and PP1α-ΔC conditions if their normalized abundance (= protein abundance divided by PP1α abundance only considering peptides that are common between PP1α-WT, PP1α−4xPR and PP1α-ΔC) was significantly (2-sided t-test, $p < 0.05$) different between the conditions. The Q values were calculated according to Benjamini-Hochberg (Supplementary Data 4). T-tests using log2 of described metrics were executed by Qlucore software.

For R2 interactomics, proteins were considered as R2 interactors if their prevalence (= protein abundance divided by total feature abundance w/o bait) displayed a fold-change higher than 2 versus the PTN-control condition. The normalized abundance is the abundance of the specific protein divided by the R2 abundance. Keratin proteins were removed from the dataset before further analysis. Phosphoproteomics of the Dox/IAA-treated HCT116 parental and R2-degron cell lines was performed as decribed by Cao et al.[42] .

Phosphoproteomics of the Dox/IAA-treated HCT116 parental and R2-degron cell lines was performed as described by Cao et al.[42]. Raw data were searched using COMET[56] against a target-decoy (reversed) version[57] of the human proteome sequence database (UniProt; downloaded 8/2020, 40704 entries of forward and reverse protein sequences; only reviewed sequences and Uniprot annotation isoform 1 were considered). Statistical analysis was carried out in Perseus[58] by two-tailed Student's t-test. In Supplementary Fig. 2c, the P-values were corrected for multiple hypotheses by permutation-based FDR correction (FDR < 0.2).

Statistics

Replicates are derived from independent experiments, unless indicated otherwise in the Fig. legends. Replicates are represented as dots shown in the quantification graphs or mentioned in the Fig. legend. To determine Vmax and K_M values, the enzymatic kinetics curves were fitted to the Michaelis-Menten equation using GraphPad Software (version 9.3.1). The IC_{50} values for inhibition of PP1α-WT and PP1α-ΔC by P_i were calculated using a four parameter logistic equation. The statistical significance of differences between 2 data sets was calculated using Student's unpaired two-tailed t-test. For the statistical analysis of more than 2 data sets, ANOVA tests were performed and multiple comparisons test, as indicated in the Fig. legends. All graphs were generated with the GraphPad Software (version 9.3.1). The exact P values are shown in Supplementary note 1 and the Source Data.

Reporting summary

Further information on research design is available in the Nature Portfolio Reporting Summary linked to this article.

Data availability

Source data are provided with this paper and were deposited at Figshare (Figshare (https://doi.org/10.6084/m9.figshare.25828345). The AlphaFold models of PP1α are publicly available from the AlphaFold Protein Structure Database (EMBL-EBI), the models of PP1:R2 (https://www.modelarchive.org/doi/10.5452/ma-6trht) and R2:PP1:RepoMan (https://www.modelarchive.org/doi/10.5452/ma-hm3cn) are available in ModelArchive. Raw MS data for the phosphoproteomics of this study are available at ProteomeXchange: PXD050733, MassIVE: MSV000094347 [https://massive.ucsd.edu/ProteoSAFe/dataset.jsp?task=7fa2a943422148c19d91e017a0caf990]; access code: p211. The mass spectrometry interactome proteomics data have been deposited to the ProteomeXchange Consortium via the PRIDE partner repository with the dataset identifier PXD052317.

References

1. Brautigan, D. L. & Shenolikar, S. Protein serine/threonine phosphatases: keys to unlocking regulators and substrates. *Annu. Rev. Biochem.* **87**, 921–964 (2018).
2. Egloff, M. P., Cohen, P. T. W., Reinemer, P. & Barford, D. Crystal structure of the catalytic subunit of human protein phosphatase 1 and its complex with tungstate. *J. Mol. Biol.* **254**, 942–959 (1995).
3. Goldberg, J. et al. Three-dimensional structure of the catalytic subunit of protein serine/threonine phosphatase-1. *Nature* **376**, 745–753 (1995).
4. Heroes, E. et al. The PP1 binding code: a molecular-lego strategy that governs specificity. *FEBS J.* **280**, 584–595 (2013).
5. Wu, D. et al. A substrate-trapping strategy for protein phosphatase PP1 holoenzymes using hypoactive subunit fusions. *J. Biol. Chem.* **293**, 15152–15162 (2018).
6. Terrak, M., Kerff, F., Langseimo, K., Tao, T. & Dominguez, R. Structural basis of protein phosphatase 1 regulation. *Nature* **429**, 780–784 (2004).
7. Bertran, M. T. et al. ASPP proteins discriminate between PP1 catalytic subunits through their SH3 domain and the PP1 C-tail. *Nat. Commun.* **10**, 771 (2019).
8. Ceulemans, H., Beke, L. & Bollen, M. Approaches to defining the ancestral eukaryotic protein complexome. *Bioessays* **28**, 316–324 (2006).
9. Lemaire, S. & Bollen, M. Protein phosphatase-1: dual activity regulation by Inhibitor-2. *Biochem. Soc. Trans.* **48**, 2229–2240 (2020).
10. Huang, F. L. & Glinsmann, W. H. Separation and characterization of two phosphorylase phosphatase inhibitors from rabbit skeletal muscle. *Eur. J. Biochem.* **70**, 419–426 (1976).
11. Marsh, J. A. et al. Structural diversity in free and bound states of intrinsically disordered protein phosphatase 1 regulators. *Structure* **18**, 1094–1103 (2010).
12. Hurley, T. D. et al. Structural basis for regulation of protein phosphatase 1 by inhibitor-2. *J. Biol. Chem.* **282**, 28874–28883 (2007).
13. Terry-Lorenzo, R. T. et al. Neurabins recruit protein phosphatase-1 and inhibitor-2 to the actin cytoskeleton. *J. Biol. Chem.* **277**, 46535–46543 (2002).
14. Dancheck, B. et al. Molecular investigations of the structure and function of the protein phosphatase 1-spinophilin-inhibitor 2 heterotrimeric complex. *Biochemistry* **50**, 1238–1246 (2011).
15. Alessi, D. R., Street, A. J., Cohen, P. & Cohen, P. T. W. Inhibitor-2 functions like a chaperone to fold three expressed isoforms of mammalian protein phosphatase-1 into a conformation with the specificity and regulatory properties of the native enzyme. *Eur. J. Biochem.* **213**, 1055–1066 (1993).
16. Huang, H. Bin et al. Characterization of the inhibition of protein phosphatase-1 by DARPP-32 and inhibitor-2. *J. Biol. Chem.* **274**, 7870–7878 (1999).
17. Tung, H. Y. L. & Cohen, P. The protein phosphatases involved in cellular regulation. Comparison of native and reconstituted Mg-ATP-dependent protein phosphatases from rabbit skeletal muscle. *Eur. J. Biochem.* **145**, 57–64 (1984).
18. Price, D. J., Tabarini, D. & Li, H.-C. Purification, subunit composition and regulatory properties of the ATP. Mg2+-dependent form of type I phosphoprotein phosphatase from bovine heart. *Eur. J. Biochem.* **158**, 635–645 (1986).
19. Vandenheede, J. R. et al. Conversion of active protein phosphatase to the ATP-Mg-dependent enzyme form by inhibitor-2. *FEBS Lett.* **127**, 1–3 (1981).
20. Bollen, M., DePaoli-Roach, A. A. & Stalmans, W. Native cytosolic protein phosphatase-1 (PP-1S) containing modulator (inhibitor-2) is an active enzyme. *FEBS Lett.* **344**, 196–200 (1994).
21. Hou, H. et al. Synaptic NMDA receptor stimulation activates PP1 by inhibiting its phosphorylation by Cdk5. *J. Cell Biol.* **203**, 521–535 (2013).

22. Foley, K. et al. Protein phosphatase-1 inhibitor-2 promotes PP1 γ positive regulation of synaptic transmission. *Front. Synaptic Neurosci.* **14**, 1021832 (2022).
23. Satinover, D. L., Leach, C. A., Stukenberg, P. T. & Brautigan, D. L. Activation of Aurora-A kinase by protein phosphatase inhibitor-2, a bifunctional signaling protein. *Proc. Natl. Acad. Sci. USA* **101**, 8625–8630 (2004).
24. Sami, F. et al. Molecular basis for an ancient partnership between prolyl isomerase Pin1 and phosphatase inhibitor-2. *Biochemistry* **50**, 6567–6578 (2011).
25. Natsume, T., Kiyomitsu, T., Saga, Y. & Kanemaki, M. T. Rapid protein depletion in human cells by auxin-inducible degron tagging with short homology donors. *Cell Rep.* **15**, 210–218 (2016).
26. Leach, C., Eto, M. & Brautigan, D. L. Domains of type 1 protein phosphatase inhibitor-2 required for nuclear and cytoplasmic localization in response to cell-cell contact. *J. Cell Sci.* **115**, 3739–3745 (2002).
27. Tsherniak, A. et al. Defining a cancer dependency map. *Cell* **170**, 564–576 (2017).
28. Colbran, R. J., Carmody, L. C., Bauman, P. A., Wadzinski, B. E. & Bass, M. A. Analysis of specific interactions of native protein phosphatase 1 isoforms with targeting subunits. *Methods Enzymol.* **366**, 156–175 (2003).
29. Beullens, M., Van Eynde, A., Stalmans, W. & Bollen, M. The isolation of novel inhibitory polypeptides of protein phosphatase 1 from bovine thymus nuclei. *J. Biol. Chem.* **267**, 16538–16544 (1992).
30. Dohadwala, M. et al. Phosphorylation and inactivation of protein phosphatase 1 by cyclin-dependent kinases. *Proc. Natl. Acad. Sci. USA* **91**, 6408–6412 (1994).
31. Kwon, Y. G., Lee, S. Y., Choi, Y., Greengard, P. & Nairn, A. C. Cell cycle-dependent phosphorylation of mammalian protein phosphatase 1 by cdc2 kinase. *Proc. Natl. Acad. Sci. USA* **94**, 2168–2173 (1997).
32. Manzione, M. G. et al. Co-regulation of the antagonistic RepoMan:Aurora-B pair in proliferating cells. *Mol. Biol. Cell* **31**, 419–438 (2020).
33. Lindorff-Larsen, K. et al. Improved side-chain torsion potentials for the Amber ff99SB protein force field. *Proteins* **78**, 1950 (2010).
34. Zhou, Y. et al. Flexible tethering of ASPP proteins facilitates PP-1c catalysis. *Structure* **27**, 1485–1496.e4 (2019).
35. Abildgaard, A. B. et al. Co-chaperones in targeting and delivery of misfolded proteins to the 26S proteasome. *Biomolecules* **10**, 1141 (2020).
36. Pattingre, S. & Turtoi, A. BAG family members as mitophagy regulators in mammals. *Cells* **11**, 681 (2022).
37. Dixon, A. S. et al. NanoLuc complementation reporter optimized for accurate measurement of protein interactions in cells. *ACS Chem. Biol.* **11**, 400–408 (2016).
38. Claes, Z. & Bollen, M. A split-luciferase lysate-based approach to identify small-molecule modulators of phosphatase subunit interactions. *Cell Chem. Biol.* **30**, 1666–1679.e6 (2023).
39. Trinkle-Mulcahy, L. et al. Repo-Man recruits PP1 gamma to chromatin and is essential for cell viability. *J. Cell Biol.* **172**, 679–692 (2006).
40. Qian, J., Beullens, M., Lesage, B. & Bollen, M. Aurora B defines its own chromosomal targeting by opposing the recruitment of the phosphatase scaffold Repo-Man. *Curr. Biol.* **23**, 1136–1143 (2013).
41. Kumar, G. S. et al. The Ki-67 and RepoMan mitotic phosphatases assemble via an identical, yet novel mechanism. *Elife* **5**, e16539 (2016).
42. Cao, X. et al. SDS22 coordinates the assembly of holoenzymes from nascent protein phosphatase-1. *Nat. Commun.* **15**, 1–17 (2024).
43. Xu, Z. et al. Structure and function of the PP2A-shugoshin interaction. *Mol. Cell* **35**, 426 (2009).
44. Padi, S. K. R. et al. Cryo-EM structures of PP2A:B55–FAM122A and PP2A:B55–ARPP19. *Nature* **625**, 195–203 (2023).
45. Wachter, F., Nowak, R. P., Ficarro, S., Marto, J. & Fischer, E. S. Structural characterization of methylation-independent PP2A assembly guides alphafold2Multimer prediction of family-wide PP2A complexes. *J. Biol. Chem.* **300**, 107268 (2024).
46. Winkler, C. et al. The selective inhibition of protein phosphatase-1 results in mitotic catastrophe and impaired tumor growth. *J. Cell Sci.* **128**, 4526–4537 (2015).
47. Tang, X. et al. A novel ATM-dependent pathway regulates protein phosphatase 1 in response to DNA damage. *Mol. Cell. Biol.* **28**, 2559–2566 (2008).
48. Weith, M. et al. Ubiquitin-independent disassembly by a p97 AAA-ATPase complex drives PP1 holoenzyme formation. *Mol. Cell* **72**, 766–777.e6 (2018).
49. De Munter, S., Köhn, M. & Bollen, M. Challenges and opportunities in the development of protein phosphatase-directed therapeutics. *ACS Chem. Biol.* **8**, 36–45 (2013).
50. Liau, N. P. D. et al. Structural basis for SHOC2 modulation of RAS signalling. *Nature* **609**, 400 (2022).
51. Peti, W. & Page, R. Strategies to make Protein Serine/Threonine (PP1, Calcineurin) and Tyrosine Phosphatases (PTP1B) druggable: achieving specificity by targeting substrate and regulatory protein interaction sites. *Bioorg. Med. Chem.* **23**, 2781 (2015).
52. Van Dessel, N. et al. The phosphatase interactor NIPP1 regulates the occupancy of the histone methyltransferase EZH2 at Polycomb targets. *Nucleic Acids Res.* **38**, 7500–7512 (2010).
53. Abraham, M. J. et al. GROMACS: High performance molecular simulations through multi-level parallelism from laptops to supercomputers. *SoftwareX* **1–2**, 19–25 (2015).
54. Kaminski, G. A., Friesner, R. A., Tirado-Rives, J. & Jorgensen, W. L. Evaluation and reparametrization of the OPLS-AA force field for proteins via comparison with accurate quantum chemical calculations on peptides. *J. Phys. Chem. B* **105**, 6474–6487 (2001).
55. Cokelaere, C. et al. TIPRL1 and its ATM-dependent phosphorylation promote radiotherapy resistance in head and neck cancer. *Cell. Oncol.* **2023**, 1–26 (2023).
56. Eng, J. K., Jahan, T. A. & Hoopmann, M. R. Comet: an open-source MS/MS sequence database search tool. *Proteomics* **13**, 22–24 (2013).
57. Elias, J. E. & Gygi, S. P. Target-decoy search strategy for increased confidence in large-scale protein identifications by mass spectrometry. *Nat. Methods* **4**, 207–214 (2007).
58. Tyanova, S. et al. The Perseus computational platform for comprehensive analysis of (prote)omics data. *Nat. Methods* **13**, 731–740 (2016).

Acknowledgements

This project received financial support from the Research Foundation-Flanders (FWO grants G095119N/G090921N), the KU Leuven Research Fund (BOF grant C14/20/101), and NIH/NIGMS R35GM119455. We thank Dr. Masato Kanemaki (School of Life Science, Sokendai) for the parental HCT116 Tet-OsTIR1 cell line.

Author contributions

S.L. generated the data illustrated in Figs. 1–4, 5e–f, 6h and 8. M.F. obtained the data for Figs. 5e–f and 6–7. Z.C. performed the AlphaFold modeling, designed the split-luciferase and nanoBRET sensors, and acquired the data shown in Figs. 5 and 8. R.D. analyzed the R2 interactome (Fig. 4a–c) and PP1 interactome (Fig. 7a–b). M.L. generated the R2-degron cell line. X.C. assisted in the purification of PP1 (Fig. 2b). F.W. and G.V.dH. provided expert technical assistance. A.v.E. co-supervised the generation of the R2-degron cell line and the sample preparation for phosphoproteomics. E.G. and A.K. performed the phosphoproteome

analysis (Fig. 2c). M.B. and S.L. wrote the first version of the manuscript. M.B. coordinated the project. All authors read the final manuscript and agreed with its contents.

Competing interests
The authors declare no competing interests.

Additional information
Supplementary information The online version contains supplementary material available at https://doi.org/10.1038/s41467-024-54256-4.

Correspondence and requests for materials should be addressed to Mathieu Bollen.

Peer review information *Nature Communications* thanks Mark Klein, Stefan Strack and the other anonymous reviewer(s) for their contribution to the peer review of this work. A peer review file is available.